1·0   2·8   2·5

3·15   2·2

1·1   3·5
4·0   2·0

4·5   1·8

1·25   1·4   1·6

NATIONAL BUREAU OF STANDARDS
MICROCOPY RESOLUTION TEST CHART
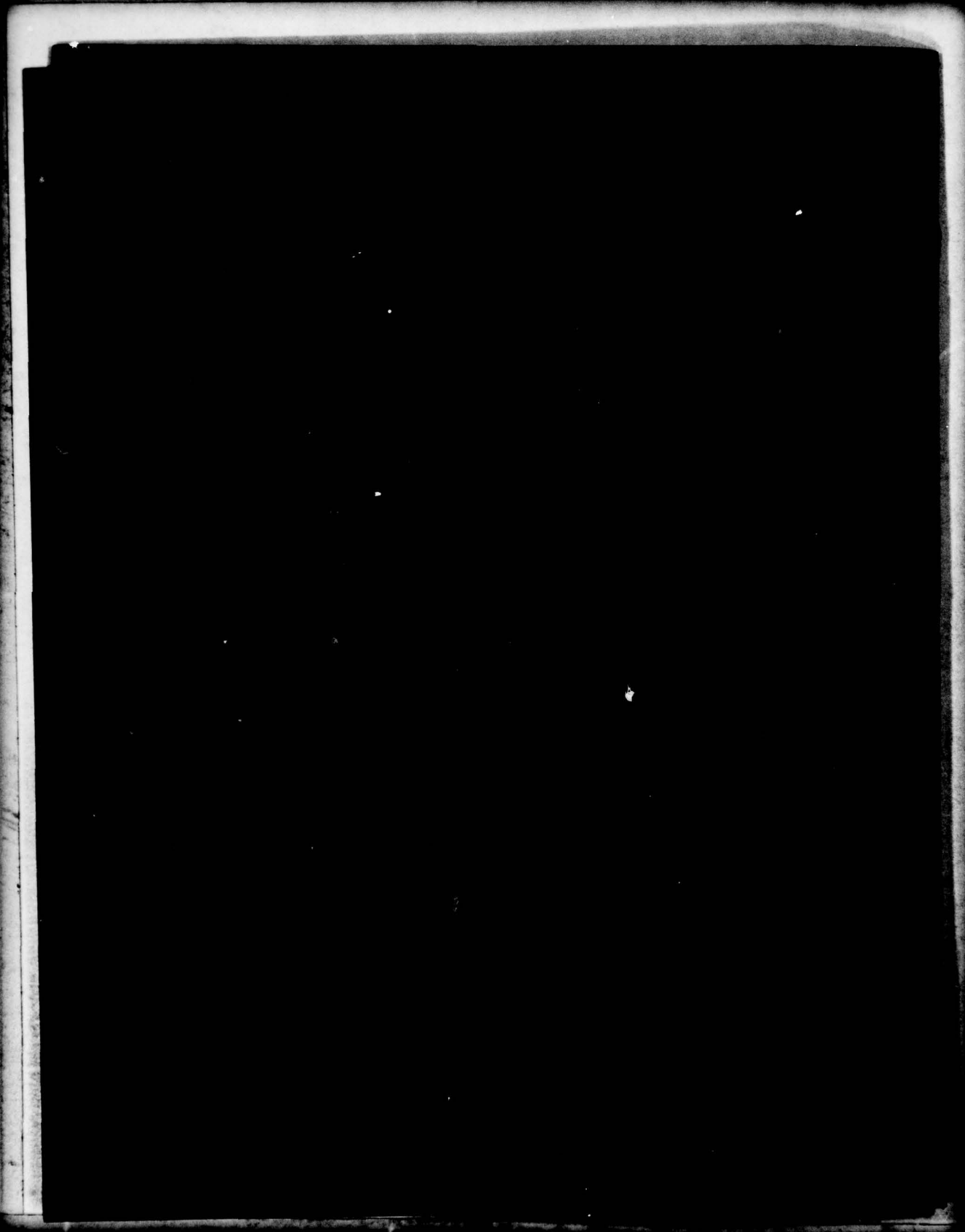
REPORT DOCUMENTATION PAGE		READ INSTRUCTIONS BEFORE COMPLETING FORM
1. REPORT NUMBER DELNV-TR-78-2450-1	2. GOVT ACCESSION NO.	3. RECIPIENT'S CATALOG NUMBER
4. TITLE (and Subtitle) PULSED RF WAVEGUIDE STUDIES PROGRAM		5. TYPE OF REPORT & PERIOD COVERED Phase 1 Report
		6. PERFORMING ORG. REPORT NUMBER FR 79-93-885
7. AUTHOR(s) L. V. Sutter		8. CONTRACT OR GRANT NUMBER(s) DAAB07-78-C-2450
9. PERFORMING ORGANIZATION NAME AND ADDRESS Laser Systems Division Electro-Optical and Data Systems Group Hughes Aircraft Co., Culver City, CA		10. PROGRAM ELEMENT, PROJECT, TASK AREA & WORK UNIT NUMBERS
11. CONTROLLING OFFICE NAME AND ADDRESS US Army ERADCOM ATTN: DELNV-L Fort Monmouth, NJ 07703		12. REPORT DATE August 1979
		13. NUMBER OF PAGES 47
14. MONITORING AGENCY NAME & ADDRESS(if different from Controlling Office)		15. SECURITY CLASS. (of this report) Unclassified
		15a. DECLASSIFICATION/DOWNGRADING SCHEDULE

16. DISTRIBUTION STATEMENT (of this Report)

Unlimited Distribution; Approved for Public Release.

17. DISTRIBUTION STATEMENT (of the abstract entered in Block 20, if different from Report)

Research and development
technical rept. Jul 78-Apr 79 on Phase 1

DDC

AUG 30 1979

A

18. SUPPLEMENTARY NOTES

19. KEY WORDS (Continue on reverse side if necessary and identify by block number)

RF Waveguide Laser
Carbon Dioxide Laser
Pulsed Waveguide Laser
RF Excitation

20. ABSTRACT (Continue on reverse side if necessary and identify by block number)

The operation of a pulsed RF Waveguide CO_2 Laser was successfully demonstrated. The efficient passive matching of the RF power supply to the laser head was achieved. Peak powers of up to 400 Watts with 150 nanoseconds pulsewidth were obtained at repetition rates of up to 20 kilohertz. Peak small signal gains of up to 2.7 percent/cm were achieved. The pulsed laser was also run CW and thus mixed mode operation is feasible.

DD FORM 1473 EDITION OF 1 NOV 65 IS OBSOLETE
1 JAN 73

408 233

TABLE OF CONTENTS

LIST OF ILLUSTRATIONS

LIST OF TABLES

INTRODUCTION

The purpose of the Pulsed RF Waveguide Studies Program, Phase 1, was to demonstrate the feasibility of and perform parametric studies on a flowing rf pumped CO_2 waveguide laser. Hughes is pleased to report the successful completion of the Phase 1 effort within the contracted time and fiscal budgets.

This report will deal with both the theoretical and experimental aspects of the program including analysis of the data and an outline of the experimental equipment and procedures used to obtain the data. Detailed derivations of the equations used in the analysis will not be included but appropriate references will be noted whenever possible to aid the reader in locating supporting background material. Descriptions of the device contained within this report will be sufficient for a basic understanding of the physics without compromising certain proprietary engineering design information obtained on internal funding.

During the course of the program, five contractual bi-monthly reports on the program progress were issued. A review of those reports illustrates the large amounts of time and monies spent during Phase 1 to eliminate a contamination problem in the laser head which would only allow for flowing gas operation such that laser output would immediately cease upon sealing off the laser head. During the interim period following the end of Phase 1 and the proposed start of Phase 2, the contamination problem was finally eliminated by changing the cleaning procedure on the laser parts prior to assembly.

The new cleaning procedure has allowed for a cw sealed-off rf wall plug efficiency of 12 percent to be obtained for the modified laser head used

1

to perform the Phase 1 experiments. (Note that a typical pulsed rf laser head may also be run cw by changing the matching network and gas mix). Unfortunately the contamination problem was not solved during Phase 1 such that all the data taken was subject to the influence of contamination although this influence was minimized by flowing the gas. The data would probably be somewhat different had the contamination issue been solved prior to data taking. Notwithstanding the results of the pulsed rf device are impressive and there is little doubt that improvements can be made in the device for the proposed Phase 2 studies.

It should also be noted that the commercial pulsed rf power supply purchased for the Phase 1 effort did not perform to specification nor was the reliability of the internal electronics acceptable. At the time of the final data taking the supply output power performance was degrading rapidly such that no more than 1.6 kW average pulse power could be obtained at the end of the experiments. The supply was specified for 2.5 kW originally. Thus most of the data was taken at low output which were not optimum in terms of laser performance. Power loading tests performed early in Phase 1 while the power supply was still operating properly indicated that average pulse power loadings to 3.0 kW was not a problem although no laser performance data was taken during this time. The point to be stressed is that the performance of the laser was at the mercy of the supply as well as the gas contamination during Phase 1 but in spite of these problems the data presented here is impressive and subsequent improvements in the device should greatly improve performance.

DEVICE DESCRIPTION

The laser used for the Phase 1 experiments was a transversely excited rf pumped CO_2 waveguide employing internal aluminum electrodes and BeO walls with gas flow into the ends of the bore and out through a hole at the center of the ground electrode. Figure 1 is a view of the laser head fully assembled including part of the matching network.

The entire laser outer shell and the electrodes were composed of cast aluminum. AR coated ZnSe windows were epoxied to each end cap thus allowing for the capability to perform gain measurements as well as power output measurements (by using an external resonator). Low vapor pressure epoxy was used in sealing the laser head. AN fittings were used to attach the gas lines to the laser head and external valves. Figure 2 illustrates the gas plumbing layout used during the experiments.

The active pumped region of the laser was 2mm x 2mm x 19 cm. The AR windows (less than 1 percent loss each) were located 2.5mm from the end of each bore opening. The ZnSe windows were 2.0mm thick. The resonator optics were located an additional 0.5mm beyond the windows. Thus the effective optical path length from the end of the discharge bore to the resonator optics was about 8.4mm at each end. The mirror separation was adjustable with a micrometer on one end. The reflectivity of the output coupling mirror was variable by interchanging optical elements. The other reflector of the resonator was 99.5 percent reflecting at 10.6 microns. The resonator was a flat-flat design. The laser head and all other peripheral optics were mounted on a rigid optical rail which itself was solidly mounted to a rigid optical table.
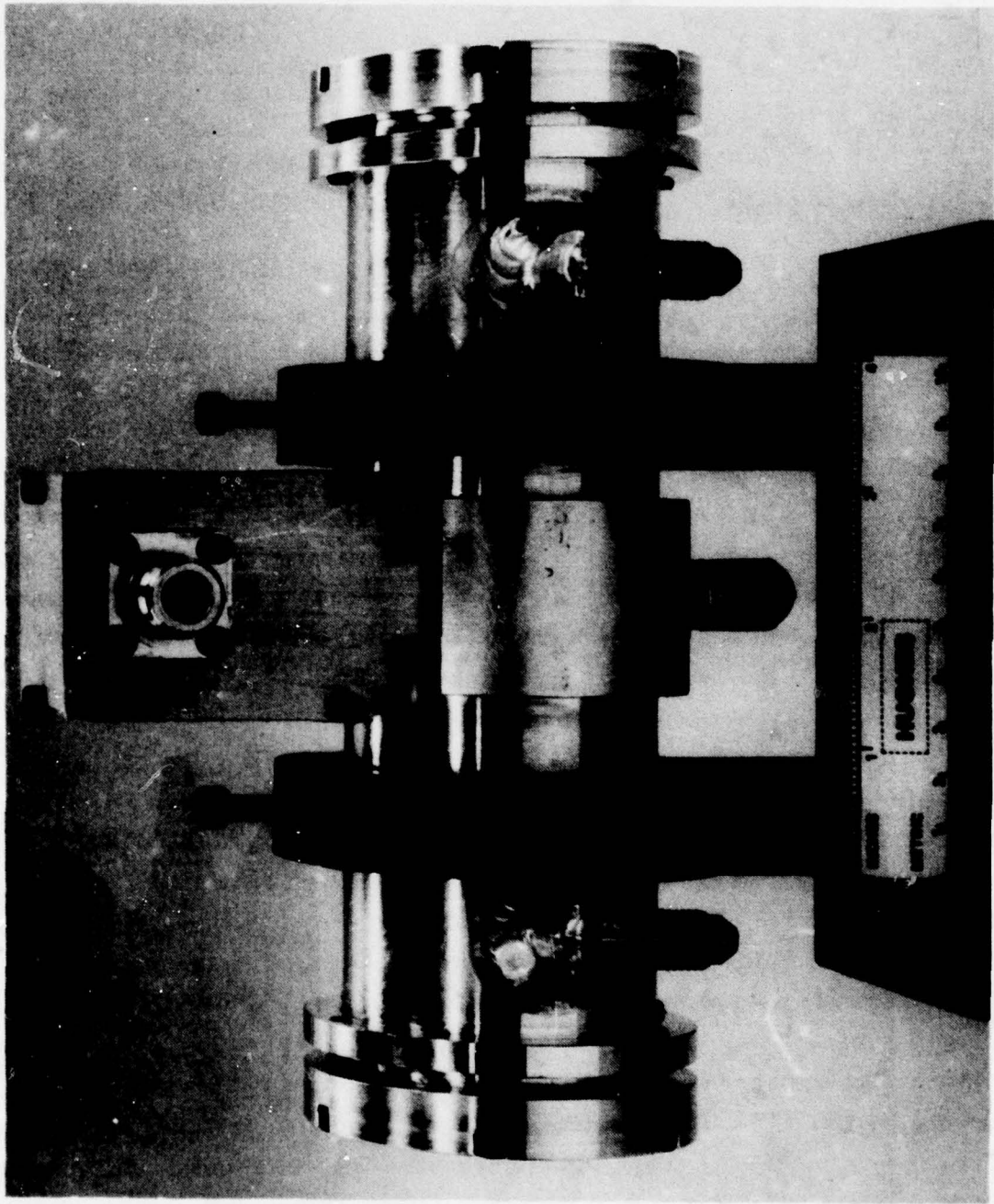
Figure 1. Pulsed RF waveguide

4
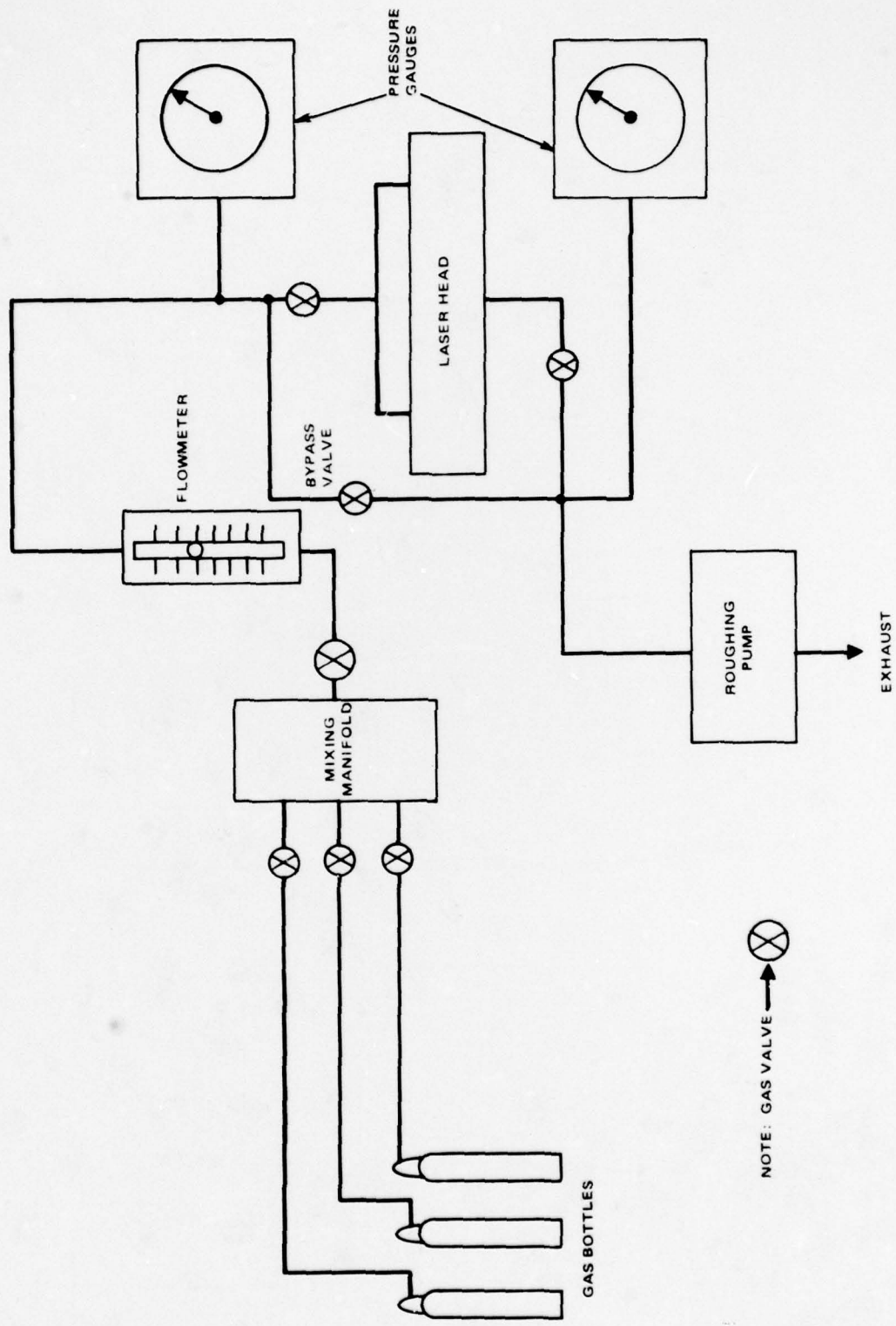
Figure 2. Gas plumbing layout

5

POWER ELECTRONICS DESCRIPTION

Figure 3 illustrates the electronics arrangement used during the experiments for loading and measuring the power delivered to and reflected from the laser head.

A 50 ohm input impedance power supply was used as the rf source. The power was delivered to the matching network through a bi-directional coupler. Two attenuated ports (-23.6 dB) from the coupler allowed for low power measurement of the forward and reflected powers. These two ports were connected to an rf switch by which either port could be connected to a second attenuator (-20 dB) and thus observed on an oscilloscope via an envelope detection circuit. The envelope detection circuit is diagrammed in Figure 4. The purpose of this device is to allow for rf noise removal due to the source (the pulse source operates at 150 MHz) by rectifying and envelope detecting the rf pulse and then band-limiting the oscilloscope to 20 MHz. The effect of this device is demonstrated in Figure 5. The circuit converts the rf pulse envelope into a rectified step function with an offset of 0.41 volts (due to the voltage drop across the diode). Thus the forward and reflected power pulses can be monitored while simultaneously using the second trace of a dual trace scope to monitor sensitive signals from the high speed infrared detector during gain and power output measurements but without rf source noise. The reflected power returning towards the generator from the load is dumped into a 50 ohm load by the use of a tuned 150 MHz circulator thus protecting the power supply during mismatched conditions. The forward power is matched into the laser head by a set of tuneable and fixed reactive elements located in the matching network and laser head.
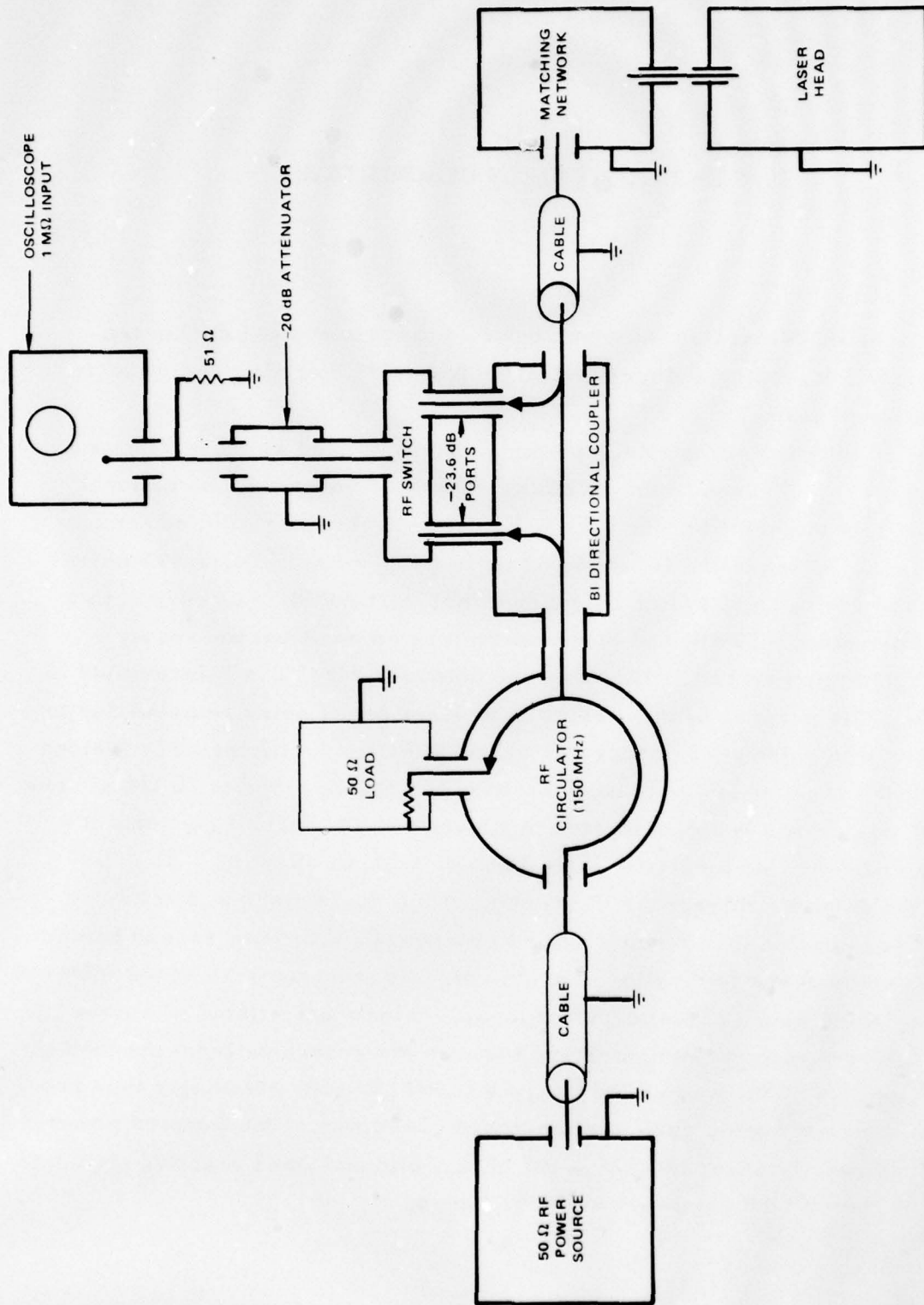
Figure 3. Power electronics layout

8

IN 5711

V_F → 51Ω   47 pF   1 KΩ   20 MHz SCOPE
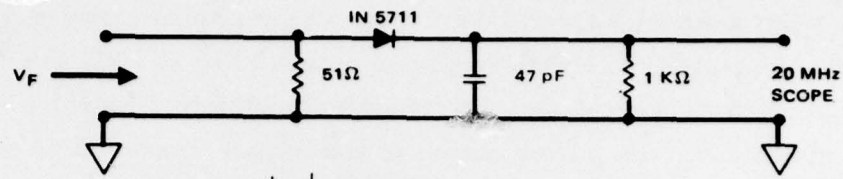
$V_{SCOPE} = |V_F| - 0.41$ VOLTS

$V_F = |V_F| \sin \omega t$

Figure 4. Envelope detection circuit

DATA TAKEN WITH
43.6 dB ATTENUATION

1.0 VOLT/DIVISION
1.0 μSEC/DIVISION
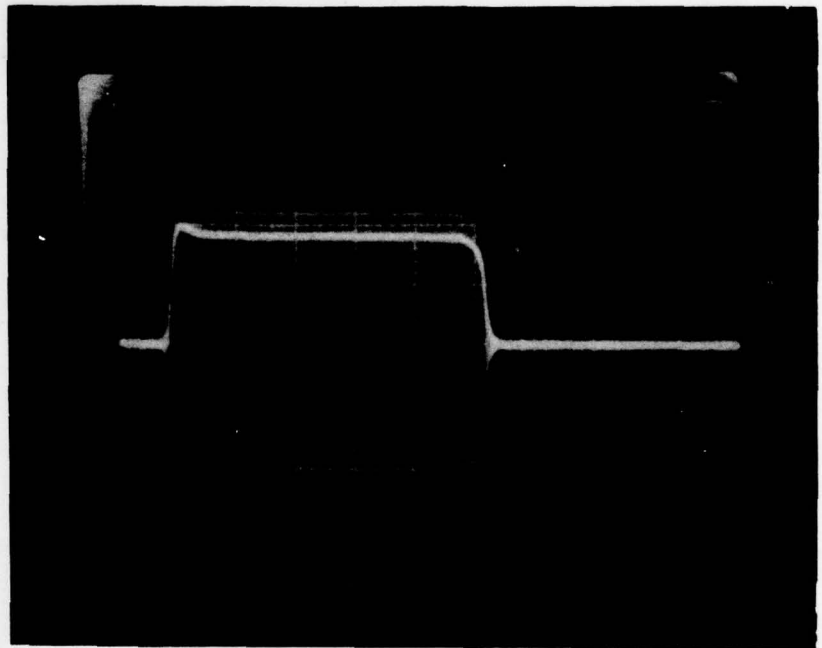
Figure 5. Typical oscilloscope traces with and without the Envelope Detection Circuit (see Figure 4.)

The pulsed power supply used as the 50 ohm source was a modified EPSCO model #5231HB1 variable in power output (0 to 2.5 kW average), pulse width (0.3 to 10 µsec), and repetition rate (0.1 to 20 kHz). As previously mentioned, the power output of the supply degraded during Phase 1 such that at the end of the primary experiments the best power obtainable from the supply was 1.6 kW.

The tuneable reactive elements in the matching network were piston-type capacitors. The pistons were driven by micrometers to improve the tuning accuracy of the capacitors.

The interconnections between the independent circuit elements was obtained with RG213 cable and N-type connectors (50 ohms). This relatively large cable diameter was chosen to minimize power losses within the cable primarily due to the skin resistance of the center conductor.

LASER HEAD ELECTRONICS MODEL

Figure 6 illustrates the lumped equivalent circuit model of the laser head. R_g represents the effective resistance of the gas during the discharge. In fact R_g is not a constant and during the power pulse will change in value such that the reflected power from the laser head will vary during the pulse. Prior to the power pulse the value of R_g can be considered nearly infinite at low pulse repetition rates (less than 20 kHz) since the residual plasma density of the previous pulse is rapidly quenched leaving a low conductivity condition. It was felt prior to Phase 1 that efficient passive matching of the power supply to the laser head in a pulsed mode would be difficult due to this temporal variation of R_g. In fact, this problem did not occur since the gas breakdown time was very rapid (less than 250 nsec) and after this breakdown time the gas resistance remained essentially constant for the rest of the pulse.
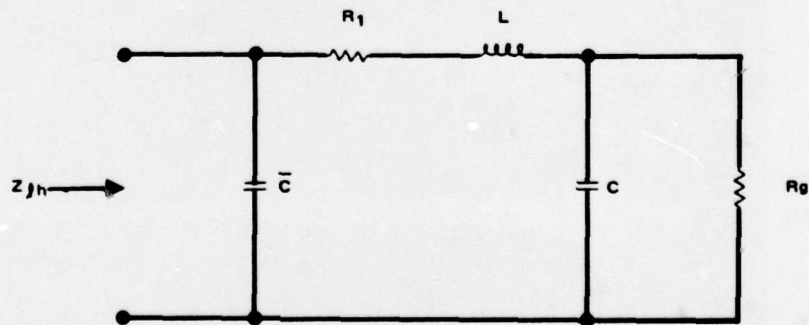
CIRCUIT VALUES FOR PULSED RF LASER

$\bar{C}$ → STRAY INPUT CAPACITANCE, ~2.4 pF
R_1 → INPUT LEAD RESISTANCE, ~0.25 Ω
L → INPUT LEAD INDUCTANCE, ~82 nH
C → DISCHARGE ELECTRODE CAPACITANCE, ~44 pF
R_g → DISCHARGE RESISTANCE, 100 TO 500 Ω TYPICAL

Figure 6. Laser head lumped circuit model

11

Figure 7 illustrates the actual forward and reflected rf envelope of the power pulse as measured with the apparatus shown in Figure 3 for a typical pulsed rf laser discharge. Note the reflected power spike at the start of the pulse which rapidly decays to a relatively low value for the duration of the pulse. Typically the reflected power after the initial spike can be held to less than 5 percent of the forward power even at powers of up to 3.0 kW. It is assumed that further increases in the power would maintain this low ratio of reflected to forward power up to the limit that gas overheating and subsequent rf arcing in the discharge occurred. The initial reflected power breakdown spike time appears to have some dependence with pulse power and generally the higher pulse powers require slightly less time for the gas to breakdown although this effect is not great.

FORWARD
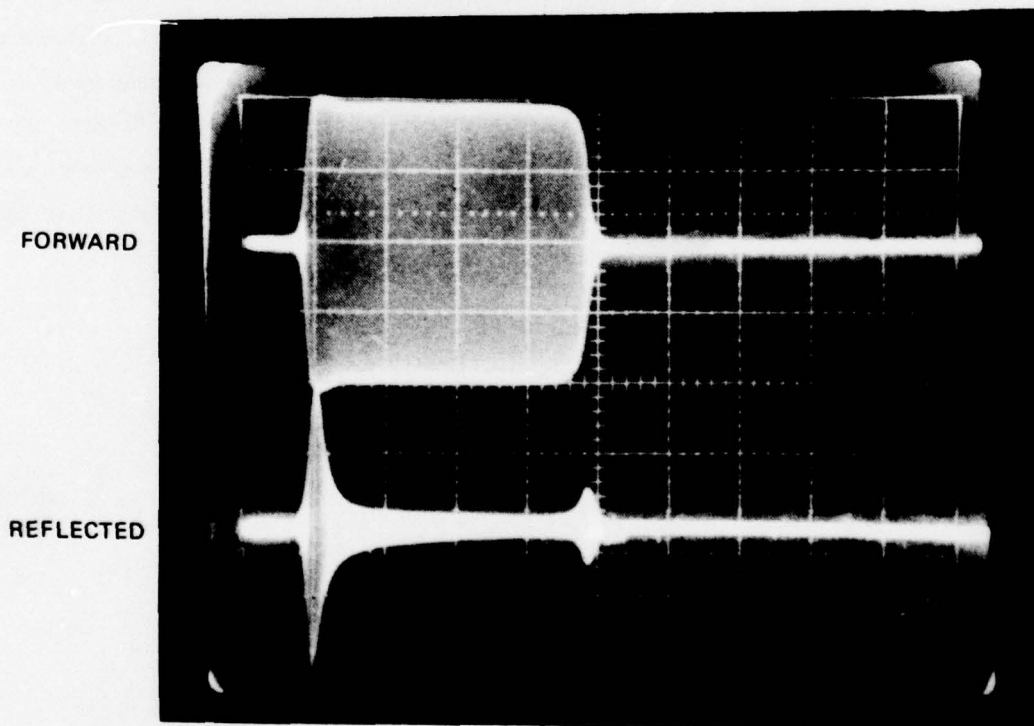
REFLECTED

DATA TAKEN WITH 43.6 dB ATTENUATION
1.0 VOLT/DIVISION
1.0 μSEC/DIVISION

Figure 7. Typical forward and reflected voltage waveforms.

12

The lumped elements in the circuit of Figure 6 were determined in the following manner. With the laser head disconnected from the matching network, a Hewlett-Packard Vector Voltmeter coupled with a low power tuneable rf source and bi-directional coupler was connected to the laser head. Without delving into the experimental aspects of this equipment, it is sufficient to say that this equipment is capable of measuring the complex reflection coefficient, ρ, of the laser head versus rf frequency (see Reference 1 for background). The complex reflection coefficient is defined as the ratio of the complex values of the reflected divided by the forward electric field vectors. The value of ρ will in general be a function of frequency which allows for the determination of the effective lumped elements of the circuit model assuming the dimensions of the laser head are much smaller than the rf wavelength. For cases where the wavelength is not much longer than the discharge length, standing wave effects will occur such that the validity of the lumped model begins to fail. The wavelength of the rf within the discharge region will also decrease by $\sqrt{\epsilon_r}$ (where ϵ_r is the relative permittivity of the ceramic waveguide walls) whenever the parallel discharge capacitance, C, is dominated by the ceramic walls. For the particular case of the pulsed rf laser used in Phase 1, BeO was used as the side wall material with $\epsilon_r = 6.8$ and the BeO was the predominate source for the capacitance, C. The discharge was 19 cm long (L_d) with the rf being center fed thus effectively reducing the electrical length by a factor of two. Thus $L_d/2 = 9.5$ cm as compared to $\lambda/\sqrt{\epsilon_r} = 76.7$ cm at 150 MHz for the discharge wavelength of the rf and thus we assert that a lumped circuit approach to the discharge model is valid.

The data obtained by the vector voltmeter for ρ is in the form of polar coordinates such that ρ is expressed as a magnitude $|\rho|$ and and angle θ. This data can then be converted into a complex impedance, $Z = R + jX$, either graphically by the use of a Smith Chart or algebraically by the relations:

$$R = Z_o \left(\frac{1 - |\rho|^2}{1 + |\rho|^2 - 2|\rho|\cos(\theta)} \right) \tag{1}$$

$$X = Z_o \left(\frac{2|\rho|\sin(\theta)}{1 + |\rho|^2 - 2|\rho|\cos(\theta)} \right) \tag{2}$$

13

where Z_o is the source impedance $\cong 50$ ohms.

Optimum matching of the rf power source to the laser head occurs when the impedance of the source as seen looking back through the matching network from the laser head is equal to the complex conjugate of the laser head impedance, Z_{1h}^*. Thus the purpose of the matching network is to transform the 50 ohms source impedance into the complex impedance Z_{1h}^* as seen by the laser head. For the lumped circuit model of Figure 6 and making the a priori assumption that this model is an accurate representation of the rf laser head, the laser head impedance, Z_{1h}, can be expressed in terms of the separate circuit elements through the equation:

$$Z_{1h} = \frac{(ac + bd) + j(da - cb)}{a^2 + b^2} \tag{3}$$

where

$$a = 1 - \omega^2 L \overline{C} - \omega^2 C \overline{C} R_g R_1$$

$$b = \omega \overline{C}(R_g + R_1) - \omega^3 L C \overline{C} R_g + \omega C R_g$$

$$c = R_1 + R_g - \omega^2 L C R_g$$

$$d = \omega L + \omega C R_1 R_g$$

$$\omega = 2\pi f$$

and where the algebra is left to the reader for verification.

DETERMINATION OF C, $\overline{C}$, AND L

By taking data of ρ for the no discharge condition ($R_g = \infty$) and assuming the capacitance across the discharge region, C, does not change appreciably between the discharge and no discharge conditions, and also assuming the laser head input lead resistance, R_1, is small, then the lumped values of C, the input lead inductance, L, and the stray input capacitance, $\overline{C}$, can be determined through the relation:

$$\frac{Z_o \sin(\theta)}{1 - \cos(\theta)} \cong \frac{1 - \omega^2 L C}{\omega^3 L \overline{C} C - \omega(\overline{C} + C)} \tag{4}$$

14

where the left side of the equation is from Equation (2) for $|\rho| = 1$. Thus by taking at least three values of ρ at three frequencies the laser head reactive lumped circuit elements can be determined. Figure 8 illustrates the match of the theoretical lumped circuit model impedance to the experimental impedance versus frequency of the laser head used in the experiments.
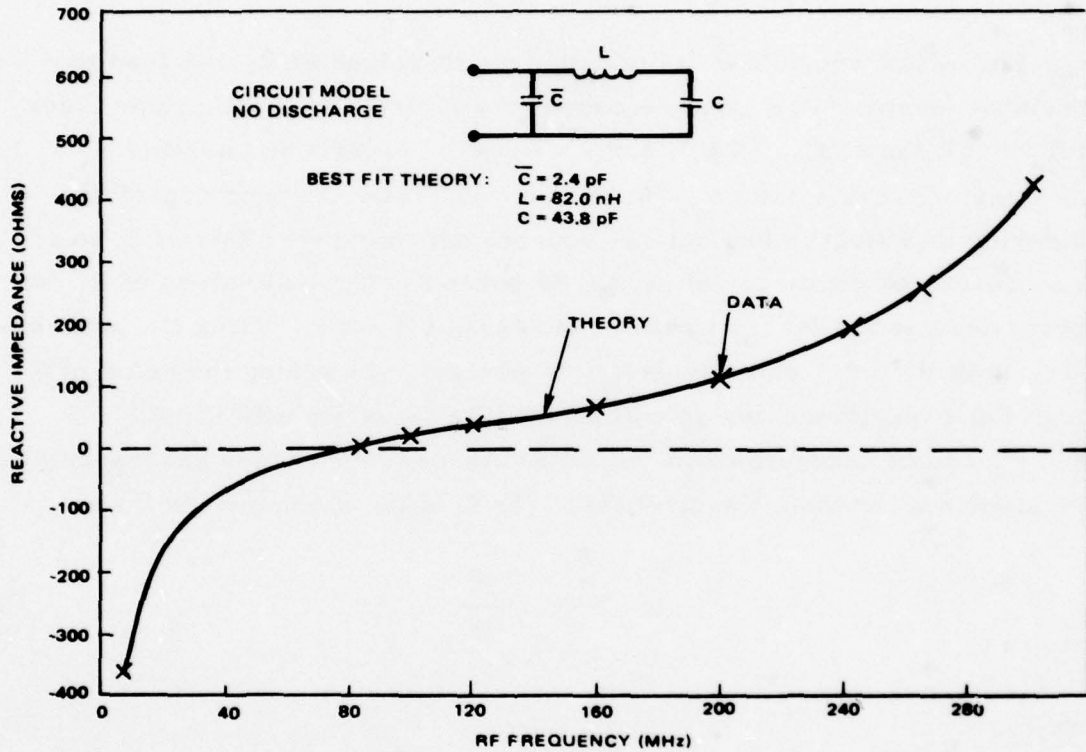
Figure 8. Theoretical vs experimental impedance for laser head, no discharge

DETERMINATION OF R_1

The input lead resistance, R_1, is a source of unwanted power losses. Even small values of R_1 can lead to significantly lowered power efficiency,

15

η_d, where η_d is defined as the ratio of the power delivered to the gas discharge divided by the total power delivered to the laser head and is given by the equation:[2]

$$\eta_d = \cfrac{1}{1 + \cfrac{R_1 (1 + \omega^2 C^2 R_g^2)}{R_g}} \tag{5}$$

For cases where C is large, even small values of R_1 can lead to appreciable losses. For example consider a typical cw rf waveguide laser with R_g = 500 ohms, C = 45 pF, and $f = \omega/2\pi$ = 150 MHz and assume R_1 = 0.5 ohms. For this case η_d = 0.69 which is relatively poor especially considering that Hughes has built rf sources which convert 28 volt dc to rf with a conversion efficiency of nearly 85 percent. Typical values of R_1 for properly designed rf lasers would be less than 0.5 ohm. Using the preceeding data with R_1 = 0.1 ohm yields η_d = 92 percent. Lowering the value of C through low capacitance design will further increase the efficiency.

R_1 can be determined in the following manner. At the resonance point of the laser head without the discharge, the Q of the laser head will be:

$$Q = \frac{\overline{\omega} L}{R} = \frac{\overline{\omega}}{\Delta \omega} \tag{6}$$

where

$$\overline{\omega} = \left(\frac{1}{LC}\right)^{1/2}$$

and where the bandwidth of the resonant circuit, $\Delta\omega$, is measured as the full width at the 3 dB points. For the pulsed laser used in the experiments, Q = 151 at $\overline{\omega} \doteq 4.6 \times 10^8$ rad/sec and L = 82 nH so that R_1 = 0.25 ohm. In general the resonance point of the laser head is not the actual operating frequency of the power source such that the value of R_1 obtained at resonance will differ slightly at the operating frequency due to the skin resistance effect which increases as the square root of frequency.

16

DETERMINATION OF R_g

The effective resistance of the gas discharge will vary with gas mix, power input, gas pressure, and rf frequency. The value of R_g for a given set of discharge parameters can be determined in the following manner. Once the reactive elements in the matching network have matched the laser head to the rf source, the impedance as seen from the laser head looking back at the source must be equal to the complex conjugate of the laser head impedance, Z_{1h}^*. For measurement purposes the rf source can be replaced by an impedance Z_o where for convenience $Z_o = 50$ ohms. It is important to note that the rf source in reality will not be exactly 50 ohms so in fact the actual rf source impedance during the discharge is not known. If $Z_{1h} = R_{1h} + iX_{1h}$ then from Equations (1) and (2) it becomes obvious that the exact value of the rf source impedance need not be known in order to determine R_g since the ratio R_{1h}/X_{1h} is independent of Z_o so that experimentally:

$$K = R_{1h}/X_{1h} = \frac{-(1 - |\rho|^2)}{2|\rho| \sin(\theta)} \tag{7}$$

Theoretically the value of K from Equation (3) is given by:

$$K = + \frac{ac + bd}{da - cb} \tag{8}$$

and thus by iterating Equation (8) on R_g using the previously determined values of R_1, C, $\overline{C}$, and L, the value of R_g can be determined. For the pulsed rf laser used in these experiments for a pulsed rf discharge in a flowing 8:1:1 mix of $He:N_2:CO_2$ at 100 Torr with an average pulse power of 1.1 kW, K was determined experimentally to be 0.079. Using the lumped circuit parameters of the laser head listed in Figure 7 and iterating Equation (8) yields a value of $R_g = 165$ ohms. The rms voltage across the discharge can then be calculated using the relation:

$$\eta_d P_{\ell h} = V^2_{rms}/R_g \tag{9}$$

17

where $P_{\ell h}$ is the average pulse power delivered to the laser head, V_{rms} is the rms pulse voltage across the discharge, and η_d is defined by Equation (5). Using the circuit elements of Figure 6 at 150 MHz, $V_{rms} = 410$ volts assuming $\eta_d = 0.93$.

DETERMINATION OF N_e

Once $P_{\ell h}$ and V_{rms} are determined, the electron number density, N_e, during the pulse can be estimated using the relation:

$$\eta_d P_{\ell h}/V_{rms} = I_{rms} = qN_e v_d A \qquad (10)$$

where I_{rms} is the rms discharge current density, q is the electron charge, v_d is the average electron drift velocity, and A is the discharge area.

The value of v_d will vary with E/N and gas mix since on the molecular level it involves the effect of collisions of electrons and molecules having different energies and collision cross-sections. The relationship of v_d to E/N can be calculated using the Boltzmann transport equation in conjunction with the collision cross-sections for the various gas species. Figure 9 illustrates the dependence of v_d on E/N for various gas mixes.

Using the previous laser head data of $V_{rms} = 410$ volts and assuming $v_d = 10^7$ cm/sec and $A = 0.2$ cm x 19 cm $= 3.8$ cm^2 we obtain $N_e = 4.1$ x 10^{11} cm^3. The assumption is also implicity made that N_e will not change appreciably per half cycle of the rf power input and it is also assumed that the gas temperature is approximately 350°K such that $N \sim 2.8$ x 10^{18} cm^3.

ELECTRICAL SUMMARY

The preceeding discussion is sufficient in describing the basic electrical characteristics of rf pumped lasers. The analysis has ignored standing wave effects which occur in electrically long devices or very high frequency devices (greater than 250 MHz). The parametric gain and output power data presented later in the report will not include corresponding parametric electrical data such as the variation of R_g with discharge condition as this data was not recorded due to the fact that this data was not contractually required and the tediousness of the calculations did not warrant the investment of analysis time.

18
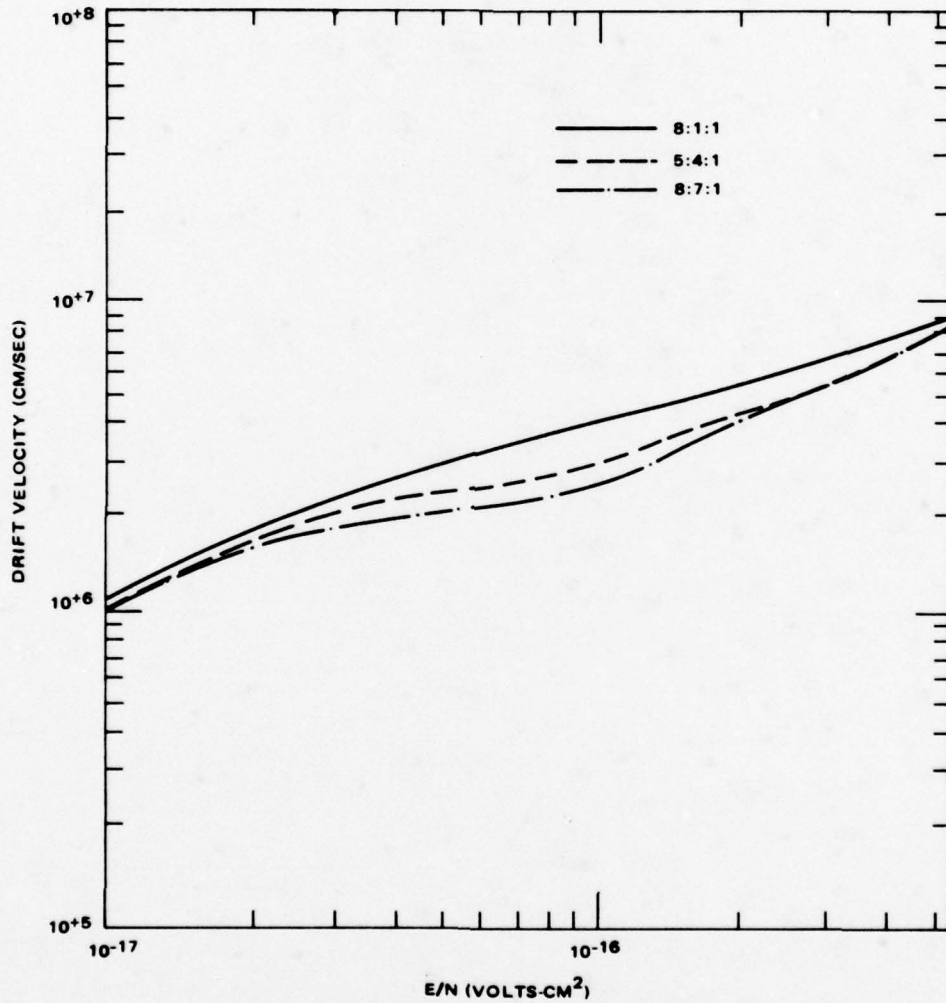
Figure 9. Electron drift velocity vs E/N for various gas mixes
(from references 3 and 4)

19

LASER CHARACTERISTICS MODEL

The following discussion will deal with a brief overview of CO_2 laser kinetics. A detailed analysis of the coupled discharge, gas thermodynamics, and laser kinetics has not been attempted due to the extreme complexity of the problem. Instead a simplified analysis of the pulsed laser performance will be discussed with a more detailed analysis to be performed during Phase 2.

LASER KINETICS MODEL

A summary of the more important CO_2 laser kinetics data and laser equations will be discussed at this time. Unless otherwise noted, this discussion is based on Reference 3.

The total stored vibrational energy above thermal equilibrium, E_s, in a mixture of CO_2 and N_2 is given by:

$$E_s \cong N(\phi_{CO_2} + \phi_{N_2})\epsilon_{001}\left(\frac{A}{1-A}\right) \quad \text{Joules/cm}^3 \tag{11}$$

where

N = the total number density of all gas species in cm^{-3}

ϕ_{CO_2} = the molar fraction of CO_2 in the gas mix

ϕ_{N_2} = the molar fraction of N_2 in the gas mix

A = the Boltzmann factor of the upper laser level

ϵ_{001} = the characteristic energy of the upper laser level which equals 4.66×10^{-20} Joules

21

The small signal 10μ band gain for a CO_2 laser mixture is given by:

$$g_o \simeq N\phi_{CO_2} (1-A)(1-B)(1-B^{1/2})^2 \sigma (g_{001,J}{}^A - g_{100,J'}{}^{B'}) \qquad (12)$$

where

B' = the Boltzmann factor for the lower 10μ band laser level

B = the characteristic Boltzmann factor of the symmetric stretch mode of the CO_2 molecules $B = B' e^{(74.8/T_g)}$

σ = the optical cross-section for the transition in cm^2

$g_{nlm,J}$ = the population fraction of the vibrational level nlm, in a particular rotational level, J

J = the rotational quantum number of the upper laser level

J' = the rotational quantum number of the lower laser level

and also noting that $B = e^{-1922/Tg}$.

The optical cross-section for the 10.6μ transition in a CO_2, N_2, and He mixture is given by:

$$\sigma = \frac{4.08 \times 10^{-17}(Tg)^{1/2}}{P(\phi_{CO_2} + 0.87 \phi_{N_2} + 0.64 \phi_{He})} \qquad (13)$$

where

P is the total gas pressure in Torr.

The rotational population fraction, $g_{1nm,K}$, is given by:

$$g_{nlm,K} = \frac{2B_{nlm}}{kTg}(2K + 1)e^{-B_{nlm}K(K + 1)/kTg} \qquad (14)$$

where

k = Boltzmann's constant = 1.38×10^{-23} Joules/$^\circ K$

B_{nlm} = the characteristic rotational energy of the vibrational mode, nlm

K = the rotational quantum number of a specific vibrational mode

and also noting that $B_{001} = 7.685 \times 10^{-24}$ Joules and $B_{100} = 7.746 \times 10^{-24}$ Joules.

22

For gas pressure in excess of 20 Torr, the laser medium is predominately pressure broadened such that the steady-state saturated gain, g, is given by the expression:

$$g = \frac{g_o}{1 + I/I_s}$$

(15)

where

I = the optical intensity in W/cm^2

I_s = the saturation intensity in W/cm^2

The 10.6μ saturation intensity is defined by the equation:

$$I_s = \frac{h\nu}{g_{001}.19^{\sigma\tau}}$$

(16)

where

h = Planck's constant = 6.626×10^{-34} Joule-sec

ν = the optical frequency in H_z

τ = the characteristic decay time of assymmetric stretch mode in μsec

The decay time, τ, is a function of gas mix, pressure, and temperature when molecular collisions dominate and is given by the equation:

$$\frac{1}{\tau} = \overline{P} \sum_i \frac{\phi_i}{\tau_i}$$

(17)

where

$\overline{P}$ = gas pressure in atm.

ϕ_i = the molar fraction of ith specie

τ_i = the decay time due to the ith specie in atm-sec.

Figure 10 gives values of τ_i versus temperature for CO_2, N_2, and He.

23
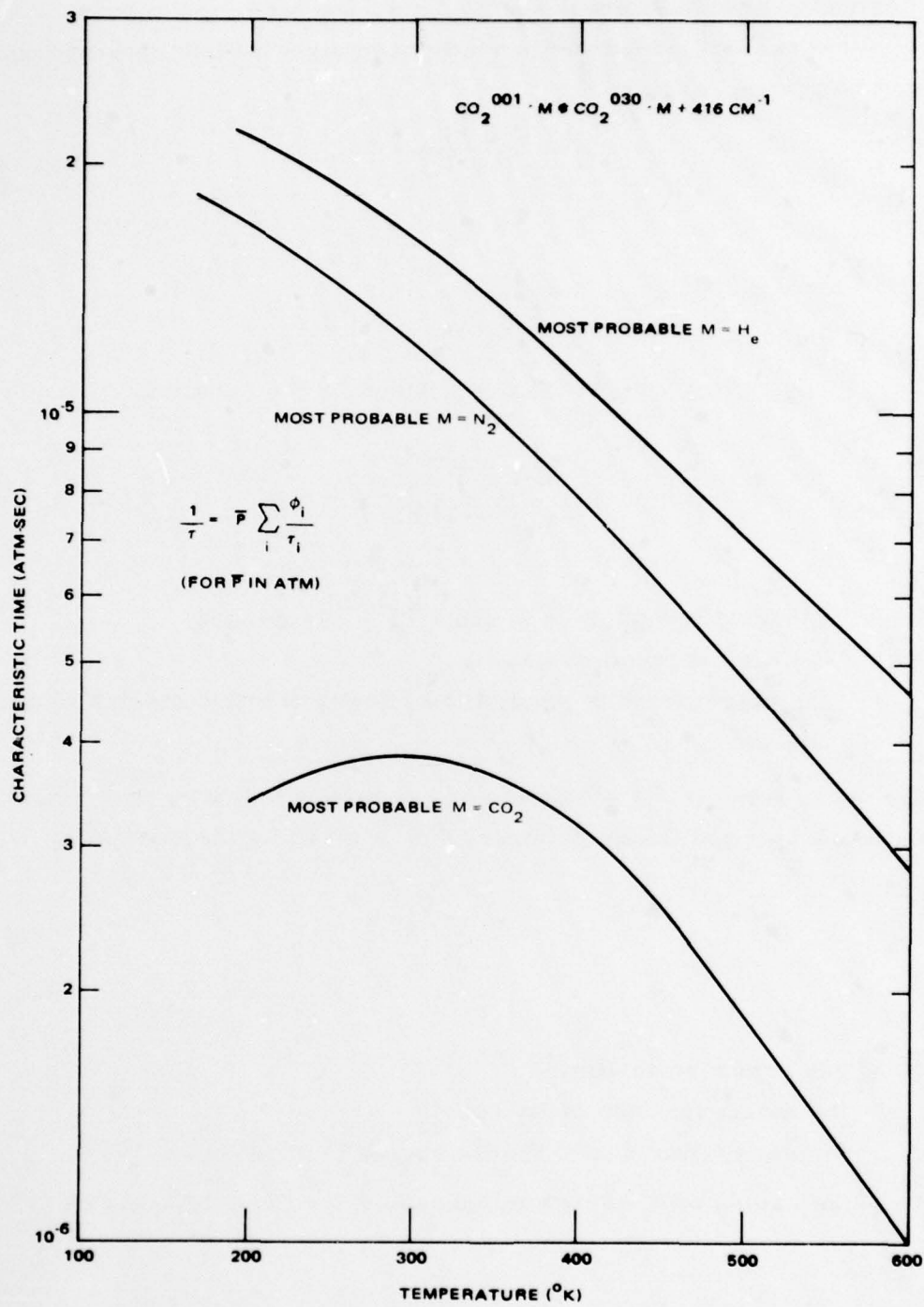
Figure 10. The characteristic decay time, τ_i, for various collision partners
(from reference 3)

24

For example, calculated values for these various parameters for an 8:1:1 ($He:N_2:CO_2$) mix at 100 Torr and $350^\circ K$ with A = 0.2 for the 10.6μ transition are given below:

$$N = 2.76 \times 10^{18}/cm^3$$
$$\nu = 2.83 \times 10^{13} Hz$$
$$\phi_{CO_2} = 0.10$$
$$\phi_{N_2} = 0.10$$
$$\phi_{H_e} = 0.80$$
$$E_s = 6.43 \times 10^{-3} J/cm^3$$
$$g_{001,19} = 6.78 \times 10^{-2}$$
$$g_{100,20} = 6.71 \times 10^{-2}$$
$$\tau = 79 \ \mu sec$$
$$I_s = 320 \ W/cm^2$$
$$\sigma = 1.09 \times 10^{-17} \ cm^2$$
$$B = 4.12 \times 10^{-3}$$
$$B' = 3.33 \times 10^{-3}$$
$$g_o = 2.8 \ percent/cm$$

POWER OUTPUT EFFICIENCY

The pulsed rf laser used in these experiments tended to produce a gain switched output spike followed by a much lower power and temporally long tail. In many respects the output resembled that of a Q-switched laser with the exception that the width of the power spike was much longer than would be expected in a Q-switched laser. In CO_2 lasers, even in the absence of N_2 or CO in the mix, the energy in higher lying levels tends to decay back to the upper laser level in times comparable to several cavity lifetimes such that the pulsewidth will be larger than predicted theoretically. The cavity lifetime is defined by the equation:[5]

$$t_c = \frac{2\ell}{c(1 - Re^{-L})} \tag{18}$$

25

where

c = the speed of light = 2.998×10^{10} cm/sec

ℓ = the cavity length in cm

R = the product of the power reflectivities of the resonator mirrors

L = the total round-trip intensity losses of the laser

The threshold gain of the laser is defined by:

$$g_{th} = \frac{1}{c\, t_c} \tag{19}$$

For cases where g_o/g_{th} is large (> 5) the theoretical pulsewidth of the Q-switch pulse is on the order of several cavity lifetimes and nearly all the inversion energy is extracted in the power pulse. A discussion of the characteristics of Q-switched lasers is given in Reference 5.

For the purposes of this discussion, we will analyze the efficiency of the pulsed rf laser in terms of the total energy extracted in the power spike and tail as compared to the input energy. The total energy stored in the upper laser levels is given by equation (11) and by:

$$E_s \cong \eta_p \, \tau_p \, \eta_d \, P_{\ell h} \tag{20}$$

where

η_p = the discharge pumping efficiency to the upper laser levels

$\eta_d P_{\ell h}$ = the rf power delivered to the discharge

τ_p = the power input pulsewidth in μsec

and where the implicit assumption is made that $\tau_p \ll \tau$ where τ is the deactivation time of the upper level vibrational mode defined by equation 17. (See References 3 and 4 for values of η_p versus E/N for several gas mixes.)

26

The total extracted energy in the output power spike can be defined by the following equation:

$$E_p = \eta_q \, \eta_e \, \eta_r \, E_s \left[\frac{\phi_{CO_2}}{\phi_{N_2} + \phi_{CO_2}} \right] \tag{21}$$

where

η_q = the quantum efficiency of the 10.6 μ transition = 0.41
η_e = the extraction efficiency
η_r = the resonator efficiency

where

η_r is defined by the equation:

$$\tag{22}$$

$$\eta_r = \frac{(1 - R)}{(1 - R) + L}$$

The value of η_e is dependent on the laser pulsewidth and the ratio of g_o/g_{th}. As previously mentioned, the theoretical value that η_e can attain is nearly 1.0 for short pulses with high values of g_o/g_{th}. For output pulses much longer than t_c, η_e will approach the approximate value:

$$\eta_e \approx \frac{g_o - g_{th}}{g_o} \tag{23}$$

and it is assumed that this approximation is valid for the pulsed rf laser.

The total round trip loss, L, of the laser resonator is a combination of lumped and distributed losses. For example, bore coupling losses (see Reference 6) and distributed waveguide losses (see References 7 and 8) will occur. For the particular design used in these studies, the coupling loss is about 2 percent and the waveguide loss is estimated to be about 2 percent.

The total efficiency of the laser pulse, η_ℓ, is thus given by the expression:

$$\eta_\ell \cong \frac{E_p}{\tau_p P_{\ell h}} = \eta_d \eta_q \eta_p \eta_r \eta_e \left[\frac{\phi_{CO_2}}{\phi_{N_2} + \phi_{CO_2}} \right] \tag{24}$$

For example, consider an 8:1:1 laser mix with $L = 0.04$, $R = 0.94$, $l = 20$ cm, and $g_o = 1.5$ percent/cm. One then calculates using $\eta_d = 0.93$, $\eta_q = 0.41$, and assuming $\eta_p = 0.30$:

$$t_c = 14 \text{ nsec}$$
$$g_{th} = 0.24 \text{ percent/cm}$$
$$\eta_r = 0.60$$
$$\eta_e = 0.84$$
$$(\phi_{CO_2})/(\phi_{N_2} + \phi_{CO_2}) = 0.5$$
$$\eta_\ell \cong 0.029$$
$$E_p = 0.10 E_s$$

These numbers are typical for the high loss external resonator used in these experiments. Improved design will increase the expected overall efficiency especially by improvement in η_r and η_d.

For mixtures containing N_2, the power output tail will contain the energy stored in the N_2 molecule while the leading spike will contain the energy stored in the CO_2 upper laser level mode only. The total laser efficiency, η_t, will be equal to the sum of the energy in the power spike and in the tail divided by the total power delivered to the laser head and is approximately equal to:

$$\eta_t = \eta_d \eta_q \eta_p \eta_r \eta_e \tag{24}$$

28

The preceeding discussion has looked at the more important aspects of the laser kinetics and expected performance under the assumptions previously outlined. This discussion is not meant to be a rigorous analysis of the problem. It is intended as a guide to the general understanding of the data to be presented in the next section.

EXPERIMENTAL RESULTS

Small signal gain and extracted output power data was obtained for the pulsed rf waveguide laser. This data was obtained by parametically varying the experimental variables such as discharge pulsewidth, pulse repetition rate, input power, gas mix, gas pressure, and gas flow rate. To minimize the amount of data, the gas pressure was set to that value which produced the largest output power spike obtained for the corresponding laser extraction experiments. Also the gas flow rate was set to a maximum for the given gas pressure as limited by the gas plumbing flow constrictions. The power input was essentially fixed for the gas mixes containing N_2 to the highest power output delivered from the power supply at the 10 kHz repetition rate so that the power output results at various repetition rates could be compared at constant input power. The power input was increased for the gas mixes without N_2 due to the decreased pumping efficiency for these mixes.

GAIN DATA

Experimental Setup and Discussion

Figure 11 illustrates the experimental arrangement for the small signal gain experiments. The attenuated 5 mW beam from a Sylvania CO_2 stabilized laser was tuned to the line center of the 10.6μ P20 transition. The beam then reflected from a mirror and was focused by an f = 7.5 cm ZnSe lens into the waveguide bore. The beam passing out of the waveguide bore was imaged on the HgCdTe 10 MHz detector by placing a ZnSe lens of f = 7.5 cm at twice this distance from the laser bore and the detector thereby eliminating steering effects of the pulsed heated gas. A manually operated blocking screen was placed directly in front of pulsed device so that a zero

31
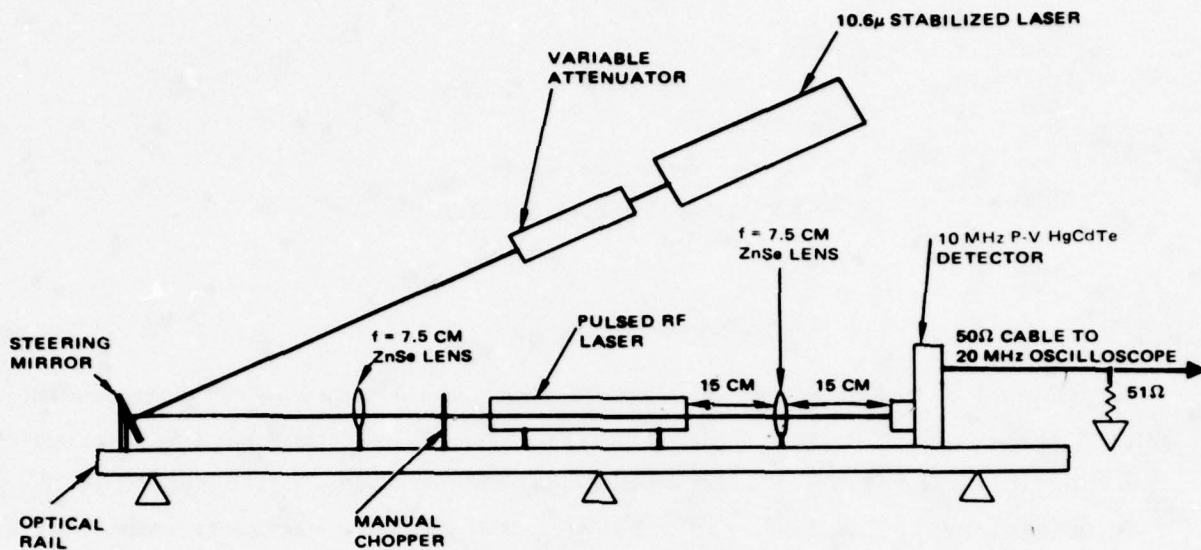
Figure 11. Small signal gain experimental apparatus

level reading could be obtained for the dc coupled detector by blocking the
probe beam. The detector was connected by a 50 ohm line to a high impedance
dual trace scope in parallel to a 51 ohm termination. The other channel of
the scope was used to record the attenuated rectified envelope of the forward
voltage signal.

Results

Data was obtained on 8:1:1, 6:2:2, and 3:0:1 (He:N_2:CO_2) gas mixes.
Only small signal gain was measured and no saturated data was taken. The
data will be presented in tabular form using the following variables to describe
the measurement data:

$P_{\ell h}$ = average pulse power into the lower head in kW

τ_p = pulsewidth of the forward power pulse in sec

f_p = the pulsewidth repetition rate in kHz

g_o = the peak measured small signal gain in cm^{-1}

τ_d = the characteristic decay time of the gain after reaching g_o
in sec

This data is presented in Table 1. Figures 12 and 13 illustrate the actual
data taken for various experimental conditions. The small signal gain versus

32

TABLE 1. TABULATED SMALL SIGNAL GAIN DATA

Gas Mix	$P_{\ell h}$ (kW)	τ_p (μsec)	f_p (kHz)	P (Torr)	$\dot{n}$ (millimoles/sec)	τ_d (μsec)	g_o (%/cm)
6:2:2	1.1	3.0	1.0	100	2.4	~80	1.8
6:2:2	1.1	6.0	1.0	100	2.4	~70	2.5
6:2:2	1.1	10.0	1.0	100	2.4	~60	2.7
6:2:2	0.6	3.0	10.0	100	2.4	~85	0.9
6:2:2	0.6	9.5	3.0	100	2.4	~80	2.5
8:1:1	1.1	3.0	1.0	100	2.4	~160	1.5
8:1:1	1.1	6.0	1.0	100	2.4	~150	2.2
8:1:1	1.1	10.0	1.0	100	2.4	~130	2.3
8:1:1	0.6	3.0	10.0	100	2.4	~130	1.4
8:1:1	0.7	9.5	3.0	100	2.4	~130	2.2
3:0:1	1.4	3.0	1.0	180	4.5	~40	1.1
3:0:1	1.4	6.0	1.0	180	4.5	~30	1.6
3:0:1	1.4	10.0	1.0	180	4.5	~30	1.8
3:0:1	1.4	3.0	3.0	180	4.5	~30	1.0
3:0:1	0.6	3.0	10.0	180	4.5	—	0.7
3:0:1	1.4	3.0	3.0	100	2.4	~50	1.2
3:0:1	1.4	10.0	1.0	100	2.4	~30	2.1
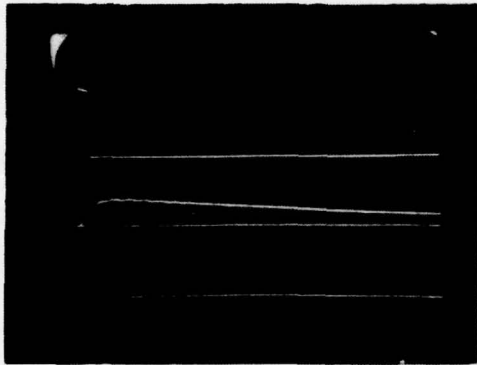
6:2:2 MIX	τ_p = 3.0 μSEC	f_p = 1.0 kHz
$P_{\ell h}$ = 1.1 kW	$\tau_d \sim$ 80 μSEC	g_o = 0.018/CM
P = 100 TORR		
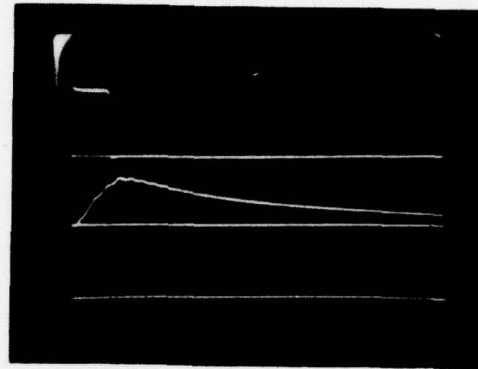
6:2:2 MIX	τ_p = 10 μSEC	f_p = 1.0 kHz
$P_{\ell h}$ = 1.1 kW	$\tau_d \sim$ 60 μSEC	g_o = 0.027/CM
P = 100 TORR		

8:1:1 MIX	τ_p = 3.0 μSEC	f_p = 1.0 kHz
$P_{\ell h}$ = 1.1 kW	$\tau_d \sim$ 160 μSEC	g_o = 0.015/CM
P = 100 TORR		
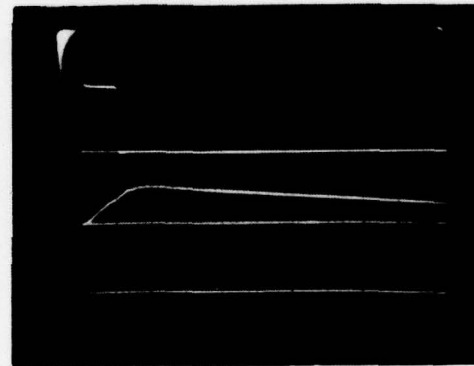
8:1:1 MIX	τ_p = 10 μSEC	f_p = 1.0 kHz
$P_{\ell h}$ = 1.1 kW	$\tau_d \sim$ 130 μSEC	g_o = 0.022/CM
P = 100 TORR		

Figure 12. Typical small signal gain data for 6:2:2 and 8:1:1 mixes at 100 torr gas pressure (Note: All photos 10 μsec/div time scale)

34
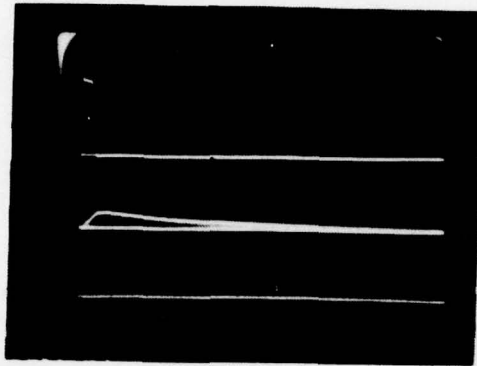
3:0:1 MIX $\tau_p = 3.0\ \mu$ SEC $f_p = 1.0$ kHz
$P_{\ell h} = 1.4$ kW $\tau_d \sim 40\ \mu$SEC $g_o = 0.011$/CM
P = 180 TORR
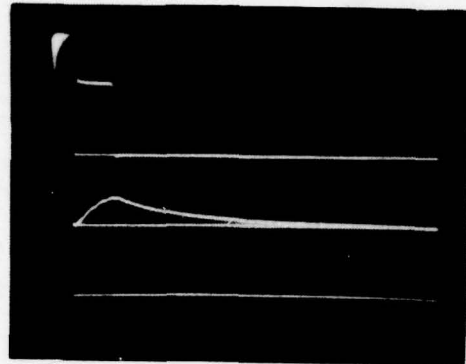
3:0:1 MIX $\tau_p = 10\ \mu$SEC $f_p = 1.0$ kHz
$P_{\ell h} = 1.4$ kW $\tau_d \sim 30\ \mu$SEC $g_o = 0.018$/CM
P = 180 TORR
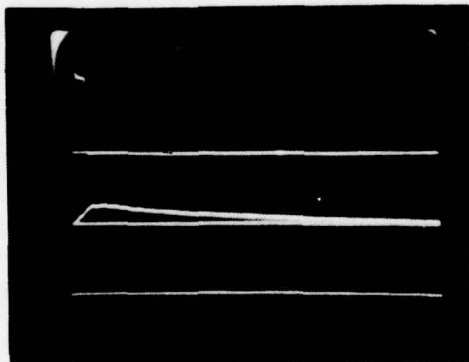
3:0:1 MIX $\tau_p = 3.0\ \mu$SEC $f_p = 1.0$ kHz
$P_{\ell h} = 1.4$ kW $\tau_d \sim 50\ \mu$SEC $g_o = 0.012$/CM
P = 100 TORR
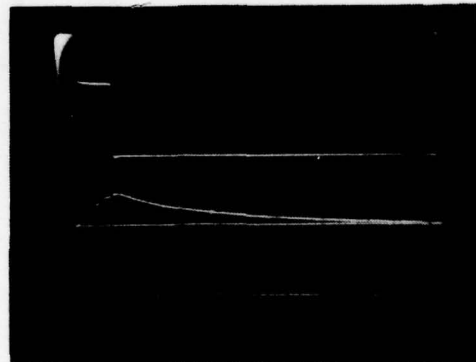
3:0:1 MIX $\tau_p = 10\ \mu$SEC $f_p = 1.0$ kHz
$P_{\ell h} = 1.4$ kW $\tau_d \sim 30\ \mu$SEC $g_o = 0.021$/CM
P = 100 TORR

Figure 13. Typical small signal gain data for 3:0:1 mix
(Note: All photos 10 μsec/div time scale)

time is illustrates in these figures and is determined by the lower three traces of each photo. The upper of the three traces is the detector signal with input power pulse to the pulsed laser. The next lower line is the detector signal without power pulse to the pulsed laser. The lowest line is the zero level of the detector. Thus these three traces determine the small signal gain of the laser medium versus time. The uppermost trace is the attenuated rectified envelope of the forward voltage pulse.

There are several interesting aspects to this data. We note that of the three mixes measured, the 6:2:2 mix had the highest g_o followed by 8:1:1 and 3:0:1 respectively. The value of g_o in nearly all the cases peaks after the power pulse as would be expected since at the end of the pulse the pumping of the lower laser level ceases thus increasing the inversion just after the pulse due to the rapid decay of this level which increases the gain. Also note that the 3:0:1 mix has the most rapid decay of the gain as compared to the other mixes. This is mostly due to the high relative CO_2 content as CO_2 molecules are more likely to deactivate excited CO_2 molecules in a collision than are He and N_2. The highest small signal gain measured was 2.7 percent/cm for the 6:2:2 mix with $f_p = 1.0$ kHz, $\tau_p = 10.0$ μsec, and $P_{\ell h} = 1.1$ kW. This does not mean that the 6:2:2 mix is the absolute best in terms of small signal gain when compared against all other $He:N_2:CO_2$ mixes. This mix was chosen as a reference to the 8:1:1 mix of which there is some published laser kinetics data. The 6:2:2 mix has twice the N_2 and CO_2 content of 8:1:1 and thus makes an interesting mix for comparative reasons.

POWER OUTPUT DATA

Experimental Setup and Discussion

Figure 14 illustrates the experimental arrangement for the power output measurements. The pulsed rf laser was operated with external optics mounted to a thermally and mechanically stable rail. AR windows at 10.6 μ were mounted to the ends of the laser shell and formed the gas seals. The gas was flowed as in the small signal gain experiments by flowing the gas through both ends of the bore and out a hole in the center of the grounded discharge electrode. The average laser output power was measured with a Coherent Radiation model #210 power meter. The actual pulse shape of the

36
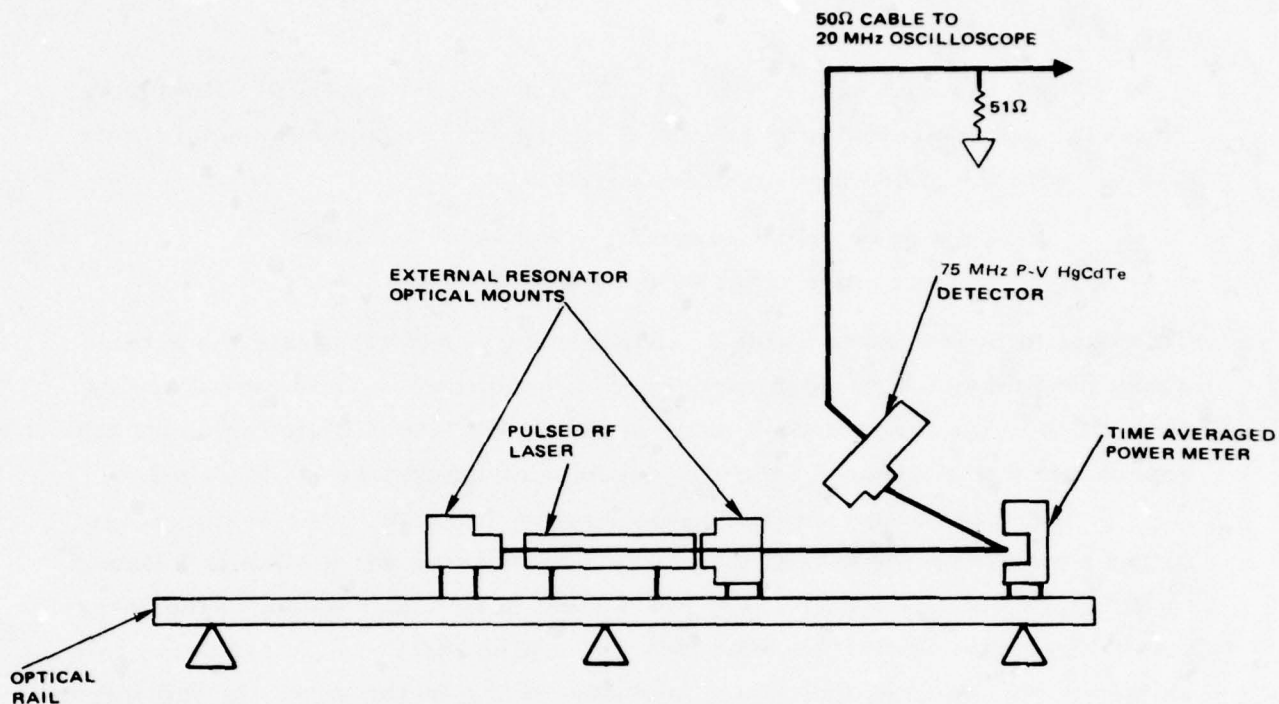
Figure 14. Power output experimental apparatus

output was measured by observing the residual scattered radiation from the power meter detector head with a 75 MHz HgCdTe detector. This detector has a 10 MHz bandwidth without the bias box (as was used in the small signal gain experiments). The detector was terminated into a dual trace high impedance scope in parallel with a 51 ohm termination. The scope was band-limited to 20 MHz to prevent rf noise signals from being displayed on the oscilloscope. The other channel of the scope was used to record the rectified envelope of the forward voltage pulse. The setting of the oscilloscope to the 20 MHz band-limit did not significantly alter the output power trace. The detector was dc coupled with a slow (10 Hz) response so that both the initial power spike and long tain in mixtures containing N_2 could be observed undis- torted. By measuring the time averaged output power and observing the fast detector trace, the peak output power was determined.

37

Results

Data was obtained on 8:1:1, 6:2:2, and 3:0:1 ($He:N_2:CO_2$) gas mixes. The data will be presented in tabular form using the same nomenclature as Table 1 with the added measurement variables:

P_p = the peak output power from the laser in Watts

P_{ave} = the average laser output power in Watts

This data is presented in Table 2. Figures 15 and 16 illustrate the actual output data taken for various experimental conditions. The lower trace in each photo is the fast detector trace of the power output while the upper trace represents the attenuated rectified envelope of the forward voltage pulse.

There are some noteworthy aspects to this data. The best average output power from the pulsed laser was obtained with the 6:2:2 mix followed by 8:1:1 and 3:0:1 respectively. The highest peak power output of the laser pulse was obtained with the 3:0:1 mix which also had the shortest decay tail as would be expected due to the absence of N_2 in the mix. In the mixes containing N_2 it is readily observed that a large fraction of the output energy occurs in the decay tail (> 50 percent). In general, the mixes containing N_2 had longer power spike pulsewidths (~ 200 to 250 nsec) as compared to the 3:0:1 mix (~150 to 200 nsec). This pulsewidth was not recorded for every parametric data point but in general the pulsewidths just mentioned were typical for all the data listed in Table 2.

The polarization of the laser output was also measured. For both cw and pulsed operation, the laser output was self-polarized such that the electric field of the laser output was parallel to the electrode surfaces. This is an important result. No Brewster windows are needed internal to the resonator and thus optical losses are minimized when polarized output is desired.

It is again important to note that the output power results would have been significantly improved had internal optics been employed. The external resonator with internal AR windows introduces significant loss both due to the window losses and the bore coupling losses which are enhanced by the large index of refraction of the ZnSe windows. The intent for Phase 2 is to use an internal resonator for the sealed-off experiments. Considering that

38

TABLE 2. TABULATED POWER OUTPUT DATA

Gas Mix	$P_{\ell h}$ (kW)	τ_p (μsec)	f_p (kHz)	P Torr	n (millimoles/sec)	R	P_p (Watts)	P_{ave} (Watts)
6:2:2	1.1	3.0	1.0	100	2.4	0.70	~220	0.20
6:2:2	1.1	6.0	1.0	100	2.4	0.70	~200	0.55
6:2:2	1.1	10.0	1.0	100	2.4	0.70	~220	0.70
6:2:2	0.6	3.0	10.0	100	2.4	0.70	~80	0.90
6:2:2	0.8	9.5	3.0	100	2.4	0.70	~130	1.55
6:2:2	1.1	3.0	1.0	100	2.4	0.80	~130	0.20
6:2:2	1.1	6.0	1.0	100	2.4	0.80	~280	0.55
6:2:2	1.1	10.0	1.0	100	2.4	0.80	~240	0.65
6:2:2	0.6	3.0	10.0	100	2.4	0.80	~80	0.70
6:2:2	0.7	9.5	3.0	100	2.4	0.80	~300	1.45
6:2:2	1.1	3.0	1.0	100	2.4	0.90	~160	0.25
6:2:2	1.1	6.0	1.0	100	2.4	0.90	~210	0.55
6:2:2	1.2	10.0	1.0	100	2.4	0.90	~210	0.65
6:2:2	0.6	3.0	10.0	100	2.4	0.90	~100	0.95
6:2:2	0.7	9.5	3.0	100	2.4	0.90	~130	1.55
8:1:1	1.1	3.0	1.0	100	2.4	0.70	~120	0.15
8:1:1	1.1	6.0	1.0	100	2.4	0.70	~130	0.35
8:1:1	1.1	10.0	1.0	100	2.4	0.70	~140	0.60
8:1:1	0.6	3.0	10.0	100	2.4	0.70	~60	0.80
8:1:1	0.7	9.5	3.0	100	2.4	0.70	~170	1.30
8:1:1	1.1	3.0	1.0	100	2.4	0.80	~140	0.15
8:1:1	1.1	6.0	1.0	100	2.4	0.80	~170	0.35
8:1:1	1.1	10.0	1.0	100	2.4	0.80	~190	0.60
8:1:1	0.6	3.0	10.0	100	2.4	0.80	~80	0.85
8:1:1	0.8	9.5	3.0	100	2.4	0.80	~190	1.15
8:1:1	1.1	3.0	1.0	100	2.4	0.90	~140	0.20
8:1:1	1.1	6.0	1.0	100	2.4	0.90	~130	0.40
8:1:1	1.1	10.0	1.0	100	2.4	0.90	~150	0.70
8:1:1	0.7	3.0	10.0	100	2.4	0.90	~80	1.20
8:1:1	0.7	9.5	3.0	100	2.4	0.90	~130	1.45
3:0:1	1.7	3.0	1.0	180	4.5	0.95	~400	0.10
3:0:1	1.7	6.0	1.0	180	4.5	0.95	~310	0.18
3:0:1	1.7	3.0	3.0	180	4.5	0.95	~280	0.20
3:0:1	1.5	3.0	3.0	100	2.4	0.95	~170	0.18
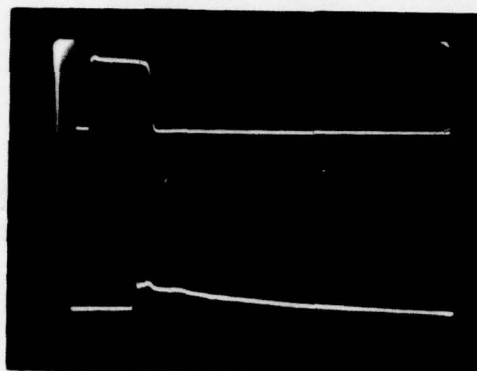
6:2:2 MIX $\tau_p = 3.0\,\mu SEC$ $f_p = 1.0\,kHz$
$P_{\ell h} = 1.1\,kW$ $P = 100\,TORR$ $P_p \sim 160W$
$R = 0.90$

6:2:2 MIX $\tau_p = 10\,\mu SEC$ $f_p = 1.0\,kHz$
$P_{\ell h} = 1.2\,kW$ $P = 100\,TORR$ $P_p \sim 210W$
$R = 0.90$
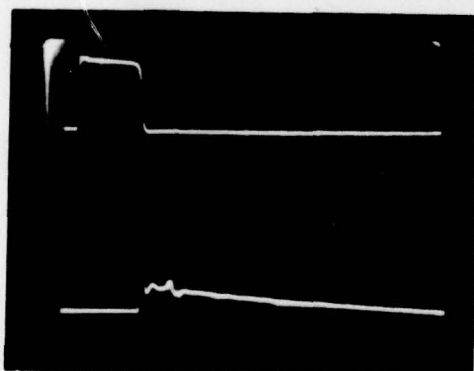
8:1:1 MIX $\tau_p = 3.0\,\mu SEC$ $f_p = 1.0\,kHz$
$P_{\ell h} = 1.1\,kW$ $P = 100\,TORR$ $P_p \sim 140W$
$R = 0.90$
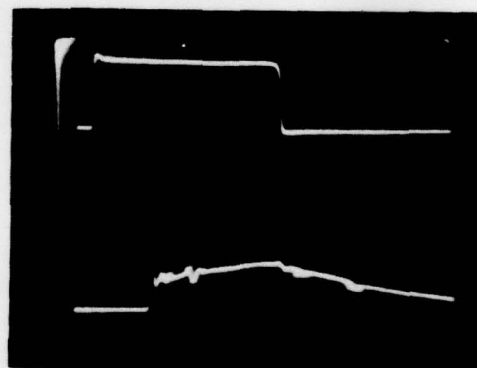
8:1:1 MIX $\tau_p = 10\,\mu SEC$ $f_p = 1.0\,kHz$
$P_{\ell h} = 1.1\,kW$ $P = 100\,TORR$ $P_p \sim 150W$
$R = 0.90$

Figure 15. Typical laser output data for 6:2:2 and 8:1:1 gas mixes at 100 torr gas pressure
(Note: All photos 2 μsec/div time scale)

40
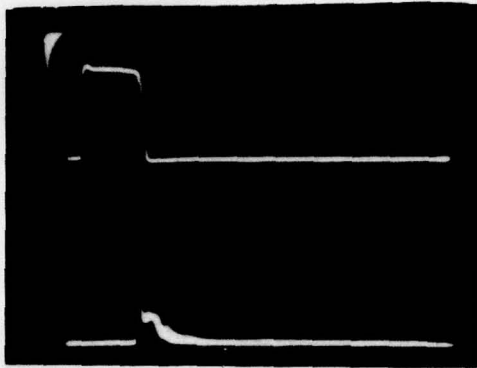
3:0:1 MIX τ_p = 3.0 μSEC f_p = 1.0 kHz
$P_{\ell h}$ = 1.7 kW   P = 180 TORR P_p ~ 400W
R = 0.95
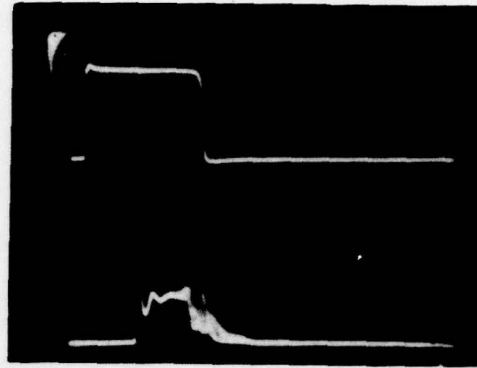
3:0:1 MIX τ_p = 6 μSEC f_p = 1.0 kHz
$P_{\ell h}$ = 1.7 kW   P = 180 TORR P_p ~ 310W
R = 0.95
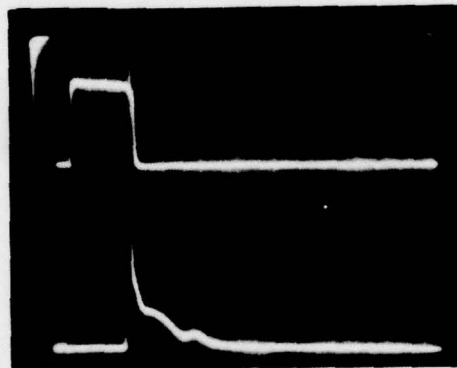
3:0:1 MIX τ_p = 3.0 μSEC f_p = 3.0 kHz
$P_{\ell h}$ = 1.5 kW   P = 100 TORR P_p ~ 150W
R = 0.95

Figure 16. Typical laser output data for 3:0:1 mix
(Note: All photos 2 μsec/div time scale)

41

the Phase 1 experiments were essentially a feasibility study of pulsed rf waveguide lasers, the results of the power output experiments are impressive.

SUMMARY

The quality of the data obtained for the Phase 1 effort is excellent. The power electronics, diagnostic equipment, monitoring electronics, and detector electronics used in taking the data performed well with the exception of the pulsed rf supply and the contamination problem of the laser head. The latter problem was overcome by flowing the gas at a rapid rate and thus parametric variation of the gas flow was not performed since decreasing the flow rate from the maximum rates used in taking the data would have led to performance degradation due to the increased effects of the contamination problem. Again it should be noted that the contamination problem has been solved since the completion of Phase 1 and thus no problem is seen in proceeding with the sealed-off experiments of Phase 2. The power supply problem is also now understood, and Hughes is making modifications to the supply which will prevent the power degradation of the supply from occurring in the future.

CONCLUSIONS AND OBSERVATIONS

Hughes has successfully demonstrated the operation of a pulsed rf waveguide CO_2 laser. There were several major results and accomplishments during this effort:

1. The efficient passive matching of the rf power supply to the laser head was demonstrated. Input powers of up to 3 kW average were achieved. Active matching networks are thus unnecessary in these devices.

2. Gain switched pulsed laser output was obtained. Peak powers of up to 400 W with 150 nsec pulsewidths were obtained with an external resonator. Repetition rates of up to 20 kHz were demonstrated. Higher rep rates are possible. Higher output powers will probably be obtained with an internal resonator.

3. Small signal gain measurements were made for the flowing gas condition. Peak small signal gains of up to 2.7 percent/cm were achieved in 6:2:2 ($He:N_2:CO_2$) flowing gas mix. The temporal decay rate of the gain was also observed and was dependent on gas mix, gas pressure, and input power.

4. The laser output was observed to be self-polarized both in pulsed and cw operation. The polarization of the optical field was observed to be parallel to the electrode surfaces. Thus no Brewster window or diffraction grating is needed to obtain polarized laser output.

5. The pulsed laser was observed to run preferentially on a lowest order mode. Changes in cavity length caused higher mode operation. The pulsed spike peak power was observed to be a maximum when the frequency of the lowest order cavity mode was situated near a gain maximum of the medium. Thus a thermally stable optical bench is necessary for these devices.

6. The pulsed laser was also run cw and thus mixed mode (both simultaneous pulsed and cw) operation is feasible.

Since the conclusion of Phase 1, sealed off operation has been obtained and the contamination problems encountered during Phase 1 have been resolved. The power supply, which had not performed properly during Phase 1, has now been fixed and thus higher input power studies can be performed. The next major effort in the development of the pulsed rf devices will be in the building of miniaturized, transistorized power supplies. Currently the laser head makes up only a small part of the total weight and size of the power supply-laser head integrated system.

Hughes is pleased to make this report on the successful completion of the Phase 1 effort. The results of Phase 1 indicate that the Phase 2 effort will have a high probability of success.

ACKNOWLEDGEMENTS

45

REFERENCES

1.   Ramo, Whinnery, and Van Duzer, Fields and Waves in Communication Electronics, Wiley and Sons, New York, 1965.

2.   Griffith, G., "Transverse RF Plasma Discharge Modeling", Hughes internal document no. 7311.22/27, February 1979.

3.   Sutter, L., "Analysis of Continuous Electron Gun Pre-Ionized Electric Laser Discharges", PhD dissertation at UCLA, 1977.

4.   Lowke et al, J. App. Phys., 44, 4664 (1973).

5.   Yariv, A., Introduction to Optical Electronics, Holt, Reinhart, and Winsten, 1971.

6.   Abrams, R.L., J. Quan. Elec., QE-8, 838 (1972).

7.   Marcatili, E.A., Bell Sys. Tech. J., 2071 (September 1969).

8.   Marcatili, E.A., and Schmeltzer, R.A., Bell Sys. Tech. J., 1783 (July 1964).

DISTRIBUTION LIST

(LASER REPORTS)

101 Defense Documentation Center
ATTN: DDC-TCA
Cameron Station (Bldg 5)
012 Alexandria, VA 22314

102 Director
National Security Agency
ATTN: TDL
001 Fort George G. Meade, MD 20755

104 Defense Communications Agency
Technical Library Center
Code 205 (P. A. Tolovi)
001 Washington, DC 20305

200 Office of Naval Research
Code 427
001 Arlington, VA 22217

201 CDR, Naval Ship Systems Comd
Technical Library, Rm 3 S-08
National Center No. 3
001 Washington, DC 20360

203 CIDEP Engineering & Support Dept
TE Section
PO Box 398
001 Norco, CA 91760

205 Director
Naval Research Laboratory
ATTN: Code 2627
001 Washington, DC 20375

206 Commander Naval Electronics
Laboratory Center
ATTN: Library
001 San Diego, CA 92152

Cdr, Naval Surface Weapons Center
White Oak Laboratory
ATTN: Library, Code WX-21
001 Silver Spring, MD 20910

212 Command, Control and
Communications Div
Development Center
Marine Corps Development and
Educ Comd
001 Quantico, VA 22134

213 Director, Naval Research Lab
ATTN: Code 4109, EOTPO
(Dr. MacCallum)
001 Washington, DC 20375

214 Commander, Naval Air Sys Comd
Meteorological Department
(AIR-05F)
002 Washington, DC 20361

217 Naval Air System Command
Code: AIR-5332
004 Washington, DC 20360

300 AUL/LSE 64-285
001 Maxwell, AFB, AL 36112

301 Rome Air Development Center
ATTN: Documents Library
(TILD)
001 Griffiss AFB, NY 13441

302 USAFETAC/CBTL
ATTN: Librarian
Stop 825
001 Scott AFB, IL 62225

307 AFGL/SULL
S-29
001 HAFB, MA 01731

312 —
AFEWC/EST
002 San Antonio, TX 78243

314 HQ, Air Force Systems Command
ATTN: DLCA
Andrews AFB
001 Washington, DC 20331

400 Cdr, MIRCOM
ATTN: DRSMI-RED
001 Redstone Arsenal, AL 35809

402 Cdr, MIRCOM
ATTN: DRSMI-RR
(Mr. Jennings)
001 Redstone Arsenal, AL 35809

403 Cdr, MIRCOM
Redstone Scientific Info Center
ATTN: Chief, Document Section
001 Redstone Arsenal, AL 35809

404 Cdr, MIRCOM
ATTN: DRSMI-RE
(Mr. Pittman)
001 Redstone Arsenal, AL 35809

406 Commandant
US Army Aviation Center
ATTN: ATZQ-D-MA
003 Fort Rucker, AL 36362

408 Commandant
US Army Military Police School
ATTN: ATSJ-CD-M-C
003 Fort McClellan, AL 36201

417 Commander
US Army Intelligence Center
and School
ATTN: ATSI-CD-MD
002 Fort Huachuca, AZ 85613

418 Commander
HQ Fort Huachuca
ATTN: Technical Reference Div.
001 Fort Huachuca, AZ 85613

422 Commander
US Army YUMA Proving Ground
ATTN: STEYP-MTD (Tech Library)
002 Yuma, AZ 85364

432 Dir, US Army Air Mobility
R&D Lab
ATTN: T. Gossett, Bldg 207-5
NASA Ames Research Center
001 Moffett Field, CA 94035

436 HQDA (DAMO-TCE)
002 Washington, DC 20310

437 Deputy For Science & Technology
Office, Assist Sec Army (R&D)
001 Washington, DC 20310

438 HQDA (DAMA-ARP)
(Dr. Verderame)
001 Washington, DC 20310

452 Cdr, US Army Training Device
Agency
ATTN: DRXPG
Naval Training Equip. Centr
001 Orlando, FL 32813

460 Cdr, ARRCOM
ATTN: DRSAR-RDP
(Library)
001 Rock Island, IL 61299

461 Cdr, Rock Island Arsenal
ARRCOM
ATTN: SARRI-LR-Y
001 Rock Island, IL 61299

466 Cdr, US Army Combined Arms
Combat Developments Activity
ATTN: ATCACC
003 Fort Leavenworth, KS 66027

470 Director of Combat Developments
US Army Armor Center
ATTN: ATZK-CD-MS
002 Fort Knox, KY 40121

474 Commander
US Army Test & Eval. Command
ATTN: DRSTE-D5-E
001 Aberdeen Proving Ground, MD

2

475 Cdr, Harry Diamond Labs
    ATTN: Library
    2800 Power Mill Road
001 Adelphi, MD 20783

476 Dir/Dev & Engr
    Defense Systems Div
    ATT: SAREA-DE-DDR
        (Mr. Tannenbaum)
002 Edgewood Arsenal, APG, MD 21010

477 Director
    US Army Ballistic Research Labs
    ATTN: DRXBR-LB
001 Aberdeen Proving Ground, MD 21005

478 Director
    US Army Ballistic Research Labs
    ATTN: DRXBR-CA
        (Dr. L. Bandekieft)
001 Aberdeen Proving Ground, MD 21005

479 Director
    US Army Human Engineering Labs
001 Aberdeen Proving Ground, MD 21005

480 Commander
    Edgewood Arsenal
    ATTN: SAREA-TS-L
001 Aberdeen Proving Ground, MD 21010

481 Harry Diamond Labs, Dept of Army
    ATTN: DRXDO-RCB
        (Dr. Nemarich)
    2800 Power Mill Road
001 Adelphi, MD 20783

482 Director
    US Army Material Systems Analysis
    Activity (ATTN: DRXSY-MP)
001 Aberdeen Proving Ground, MD 21005

498 Cdr, TARADCOM
    ATTN: DRDTA-UL,
        Technical Library
001 Warren, MI 48090

499 Cdr, TARCOM
    ATTN: DRDTA-RH
001 Warren, MI 48090

507 Cdr, AVRADCOM
    ATTN: DRSAV-E
    PO Box 209
001 St. Louis, MO 63166

511 Commander, ARRADCOM
    ATTN: DRDAR-LCA-PD
002 Dover, NJ 07801

513 Commander, ARRADCOM
    ATTN: DRDAR-TSS
001 Dover, NJ 07801

519 Cdr, US Army Avionics Lab
    AVRADCOM
    ATTN: DAVAA-D
001 Fort Monmouth, NJ 07703

518 Tri-Tac Office
    ATTN: TT-SE
        (Dr. Pritchard)
001 Fort Monmouth, NJ 07703

526 Commander
    White Sands Missile Range
    ATTN: STEWS-ID-S HQ
002 White Sands Missile Range, NM

527 Commander
    White Sands Missile Range
    ATTN: STEWS-ID-O
001 White Sands Missile Range, NM

531 Cdr, US Army Research Office
    ATTN: DRXRO-IP
    PO Box 12211
001 Research Triangle Part, NC 27709

532 Cdr, US Army Research Office
    ATTN: DRXRO-PH
        (Dr. Lontz)
    PO Box 12211
001 Research Triangle Park, NC 27709

536 Commander
US Army Arctic Test Center
ATTN: STEAC-TD-MI
002 APO Seattle, WA 98733

537 Cdr, US Army Tropic Test Center
ATTN: STETC-MO-A
(Tech Library)
Drawer 942
001 Fort Clayton, Canal Zone 09827

542 Commandant
US Army Field Artillery School
ATTN: ATSFA-CTD
002 Fort Sill, OK 73503

554 Commandant
US Army Air Defense School
ATTN: ATSA-CD-MC
001 Fort Bliss, TX 79916

555 Commander
US Army Nuclear & Chemical Agency
7500 Backlick Road, Building 2073
001 Springfield, VA 22150

556 HQ TCATA
Technical Information Center
ATTN: Mrs. Ruth Reynolds
001 Fort Hood, TX 76544

559 Commander
US Army Dugway Proving Ground
ATTN: MT-T-M
001 Dugway, UT 84022

562 Commander, DARCOM
ATTN: DRCDE-DE
(Mr. Bladgett)
5001 Eisenhower Avenue
001 Alexandria, VA 22333

563 Commander, DARCOM
ATTN: DRCDE
5001 Eisenhower Avenue
001 Alexandria, VA 22333

564 Cdr, US Army Signals
Warfare Lab
ATTN: DELSW-OS
Vent Hill Farms Station
001 Warrenton, VA 22186

567 Commandant
US Army Engineer School
ATTN: ATSE-TD-TL
002 Fort Belvoir, VA 22060

568 Commander
US Army Mobility Eqp Res
and Dev Cmd
ATTN: DRXFB-R
001 Fort Belvoir, VA 22060

569 Commander
US Army Engineer Topographic
Labs (ATTN: ETL-TD-EA)
001 Fort Belvoir, VA 22060

571 Director, Eustis Directorate
US Army Air Mobility R&D Lab
ATTN: Technical Library
001 Fort Eustis, VA 23604

572 Commander
US Army Logistics Center
ATTN: ATCL-MC
002 Fort Lee, VA 22801

573 Commander
US Army Logistics Center
ATTN: ATCL-MA
001 Fort Lee, VA 23801

574 Commander
HQ, TRADOC
ATTN: ATTNG-XO
002 Fort Monroe, VA 23651

575 Commander
US Army Training
and Doctrine Cmd
ATTN: ATCD-TEC
001 Fort Monroe, VA 23651

576 Commander
US Army Training & Doctrine Cmd
ATTN: ATCD-SIE
001 Fort Monroe, VA 23651

578 Cdr, US Army Garrison
Vint Hill Farms Station
ATTN: IAVAAF
001 Warrenton, VA 22186

600 Director, Night Vision Lab
US Army Electronics Command
ATTN: DRSEL-NV-VIS
        (Mr. L. Gillespie)
001 Fort Belvoir, VA 22060

601 Director, Night Vision Lab
US Army ERADCOM
ATTN: DELNV-SD
        (Mr. Gibson)
001 Fort Belvoir, VA 22060

602 Director, Night Vision Lab
US Army ERADCOM
ATTN: DELNV-D
001 Fort Belvoir, VA 22060

604 Chief
Ofc of Missile Electronic Warfare
Electronic Warfare Lab, ERADCOM
001 White Sands Missile Range,
New Mexico 88002

606 Chief
Intel Material Dev & Spt Ofc
Electronic Warfare Lab, ERADCOM
001 Fort Meade, MD 20755

680 Commander
US Army Electronics Research
and Development Command
Fort Monmouth, NJ 07703

1 DELSD-D-PC
ATTN: J. Sanders
1 DRSEL-PL-ST
1 DELEW-D

1 DELAS-D
1 DELNV-L
(Dr. R. G. Buser)
1 DELNV-L-E
(Dr. H. Hieslmair)
1 DELNV-L-D
(Mr. J. Strozyk)
1 DELET-D
1 DELET-I
(Dr. Jacobs)
1 DELET-B
1 DELET-TG
(Mr. S. Schneider)
1 DRDCO-COM-RM-1
(Dr. E. Dworkin)
1 DELEW-SW
1 DRSEL-MA-MP
2 DELSD-L-S
1 DELSD-L
2 DRSEL-PA
1 DRDEL-SA
(Dr. McAfee)
DELNV-L
(Originating Office)
1 DRCPM-TDS-SE
1 USMC-LNO

700 CINDAS
Purdue Industrial Research Park
2595 Yeager Road
001 W. Lafayette, IN 47096

701 MIT - Lincoln Laboratory
ATTN: Library (Rm A-082)
PO Box 73
002 Lexington, MA 02173

702 Environmental Research Inst.
of Michigan
ATTN: IRIA Library
PO Box 618
001 Ann Arbor, MI 48107

703 NASA Scientific & Tech Info Fac.
Baltimore/Washington
Intl Airport
001 PO Box 8757, MD 21240

5

706 Advisory Group on Electron Dev
ATTN: Secy, Working Group D
(Lasers)
201 Varick Street
002 New York, NY 10014

707 TACTEC
Battelle Memorial Institute
505 King Avenue
001 Columbus, OH 43201

709 Plastics Tech Eval Center
Picatinny Arsenal, Bldg 176
ATTN: Mr. A.M. Anzalone
001 Dover, NJ 07801

710 Ketron, Inc.
ATTN: Mr. Frederick Leuppert
1400 Wilson Blvd, Architect Bldg
002 Arlington, VA 22209

711 Metals and Ceramics Inf. Center
Battelle
505 King Avenue
001 Columbus, OH 43201

Commanding General
US Army ERADCOM
2800 Powder Mill Road
Adelphi, MD 20783

ATTN: DRDEL-CG/DRDEL-DC/
        DRDEL-CS
        DRDEL-CT (2 cys)
        DRDEL-PAO
        DRDEL-SB/
        DRDEL-EA
        DRDEL-AP (2 cys)
        DRDEL-PA/DRDEL-ILS/
        DRDEL-E
        DRDEL-TD (Dr. W. Carter)

Commander
Harry Diamond Laboratories
ATTN: DELHD-CO
2800 Power Mill Road
Adelphi, MD 20783

Commander
Department of the Army
Project Manager, FIREFINDER
ATTN: DRCPM-FF
Fort Monmouth, NJ 07703

Commander
Department of the Army
Project Manager, SOTAS
ATTN: DRCPM-STA
Fort Monmouth, NJ 07703

Commander
Department of the Army
Project Manager,
Concept Analysis Centers
ATTN: DRCPM-CAC
Arlington Hall Station
Arlington, VA 22212

Commander
Aviation Flight Test Activity
ATTN: DELAF-CO
Lakehurst NAEC, NJ 08733